



## Article (refereed) – Published version

---

Naveira Garabato, Alberto C.; Nurser, A.J. George; Scott, Robert B.; Goff, John A..  
2013 The Impact of Small-Scale Topography on the Dynamical Balance of the  
Ocean. *Journal of Physical Oceanography*, 43 (3). 647-668. [10.1175/JPO-D-12-056.1](https://doi.org/10.1175/JPO-D-12-056.1)

This version available at <http://nora.nerc.ac.uk/501787/>

NERC has developed NORA to enable users to access research outputs wholly or partially funded by NERC. Copyright and other rights for material on this site are retained by the rights owners. Users should read the terms and conditions of use of this material at

<http://nora.nerc.ac.uk/policies.html#access>

© Copyright 2013 American Meteorological Society (AMS).

Permission to use figures, tables, and brief excerpts from this work in scientific and educational works is hereby granted provided that the source is acknowledged. Any use of material in this work that is determined to be “fair use” under Section 107 of the U.S. Copyright Act September 2010 Page 2 or that satisfies the conditions specified in Section 108 of the U.S. Copyright Act (17 USC §108, as revised by P.L. 94-553) does not require the AMS’s permission.

Republication, systematic reproduction, posting in electronic form, such as on a web site or in a searchable database, or other uses of this material, except as exempted by the above statement, requires written permission or a license from the AMS. Additional details are provided in the AMS Copyright Policy, available on the AMS Web site located at (<http://www.ametsoc.org/>) or from the AMS at 617-227-2425 or [copyrights@ametsoc.org](mailto:copyrights@ametsoc.org).

Contact NOC NORA team at  
[publications@noc.soton.ac.uk](mailto:publications@noc.soton.ac.uk)

# The Impact of Small-Scale Topography on the Dynamical Balance of the Ocean

ALBERTO C. NAVEIRA GARABATO

*University of Southampton, National Oceanography Centre, Southampton, United Kingdom*

A. J. GEORGE NURSER

*National Oceanography Centre, Southampton, United Kingdom*

ROBERT B. SCOTT

*Laboratoire de Physique des Océans, University of Brest, France*

JOHN A. GOFF

*Institute for Geophysics, University of Texas at Austin, Austin, Texas*

(Manuscript received 22 March 2012, in final form 7 December 2012)

## ABSTRACT

The impact of small-scale topography on the ocean's dynamical balance is investigated by quantifying the rates at which internal wave drag extracts (angular) momentum and vorticity from the general circulation. The calculation exploits the recent advent of two near-global descriptions of topographic roughness on horizontal scales on the order of 1–10 km, which play a central role in the generation of internal lee waves by geostrophic flows impinging on topography and have been hitherto unresolved by bathymetric datasets and ocean general circulation models alike. It is found that, while internal wave drag is a minor contributor to the ocean's dynamical balance over much of the globe, it is a significant player in the dynamics of extensive areas of the ocean, most notably the Antarctic Circumpolar Current and several regions of enhanced small-scale topographic variance in the equatorial and Southern Hemisphere oceans. There, the contribution of internal wave drag to the ocean's (angular) momentum and vorticity balances is generally on the order of ten to a few tens of percent of the dominant source and sink terms in each dynamical budget, which are respectively associated with wind forcing and form drag by topography with horizontal scales from 500 to 1000 km. It is thus suggested that the representation of internal wave drag in general circulation models may lead to significant changes in the deep ocean circulation of those regions. A theoretical scaling is derived that captures the basic dependence of internal wave drag on topographic roughness and near-bottom flow speed for most oceanographically relevant regimes.

## 1. Introduction

The dynamical balance of the ocean's general circulation, commonly expressed in terms of the steady, depth-integrated (angular) momentum and (potential) vorticity budgets, is presently understood as a leading-order balance between an acceleration of the ocean by wind stress and a deceleration by pressure forces on the bottom topography (e.g., Hughes and de Cuevas 2001;

Vallis 2006). This may be illustrated by invoking, for example, the depth-integrated momentum equation,

$$f\mathbf{k} \times \mathbf{U} + \nabla P + \mathbf{R} = \boldsymbol{\tau}_w + p_b \nabla H - \boldsymbol{\tau}_b, \quad (1)$$

where steadiness has been assumed. In (1)  $f$  is the Coriolis parameter;  $\mathbf{k}$  is the unit vector in the vertical (upward) direction;  $\mathbf{U} = \int_{-H}^{\eta} \rho \mathbf{u} dz$  is the depth-integrated mass transport (with  $H$  as the depth of the ocean floor,  $\eta$  as the height of the ocean surface,  $\rho$  as density and  $\mathbf{u}$  as velocity);  $P = \int_{-H}^{\eta} p dz$  is the depth integral of pressure (denoted by  $p$ ); the term  $\mathbf{R}$  amalgamates contributions to the lateral redistribution of momentum by lateral viscous stresses and nonlinearities in  $\mathbf{u}$ ;  $p_b$  is the bottom pressure;  $\boldsymbol{\tau}_w$  is the

---

*Corresponding author address:* Alberto C. Naveira Garabato, University of Southampton, National Oceanography Centre, Southampton SO14 3ZH, United Kingdom.  
E-mail: acng@noc.soton.ac.uk

wind stress at the ocean surface; and  $\tau_b$  is the bottom frictional stress. The term  $\mathbf{R}$  may be locally significant but averages out to zero when integrated over a wide enough area (Hughes and de Cuevas 2001; Eden and Olbers 2009), so it can be neglected. With this approximation in place, Eq. (1) states that the component of the lateral transport of momentum not balanced by thermal wind (i.e.,  $f\mathbf{k} \times \mathbf{U} + \nabla P$ ) is locally forced by a source of momentum from the wind ( $\tau_w$ ) and sinks of momentum associated with pressure forces on the bottom topography ( $p_b \nabla H$ ) and bottom friction forces (drag) in a viscous boundary layer ( $-\tau_b$ ).<sup>1</sup> While the latter term had been portrayed as the primary (and only) momentum sink by classical theories of ocean circulation (e.g., Stommel 1948; Munk 1950), it was later argued to be largely negligible by numerous authors [see, e.g., Vallis (2006) and references therein]. Thus, the resulting momentum balance indicates that the ocean is set in motion by the wind and that its flow is ultimately arrested by a topographic form drag.

Investigations of this fundamental balance in general circulation models have confirmed its validity (Hughes and de Cuevas 2001; Eden and Olbers 2009). The models, which have resolutions ranging from eddy-permitting [ $O(10 \text{ km})$ ] to coarse [ $O(100 \text{ km})$ ], reveal the decelerating action of topographic form drag to be associated with the occurrence of pressure gradients across prominent features of the bottom topography (such as continental slope regions, major ridges and plateaus) typically measuring 500–1000 km across [see e.g., Fig. 4 in Hughes and de Cuevas 2001 or Fig. 7b in this article]. The prevalence of this length scale in the ocean momentum sink as portrayed by general circulation models may be understood by examining the (friction-based) physical mechanism mediating the setup of pressure gradients across the large-scale topographic features resolved by the models. This is done in section 2. There, it is shown that the effectiveness of topography in arresting the ocean circulation generally increases as the height, steepness, and horizontal dimensions of the topographic features increase. This would appear to imply that topography with horizontal scales comparable to or smaller than those resolved by general circulation models is ineffective at arresting the ocean circulation. However, as the horizontal scale of topography decreases, a narrow range of small horizontal scales is encountered for which topographic form drag is underpinned by

distinct, comparatively more effective physics: the generation of internal lee waves by geostrophic flow impinging on topography (e.g., Bell 1975; Gill 1982). The horizontal dimensions of the small-scale topography implicated in lee wave generation typically range from hundreds of meters to up to  $O(10 \text{ km})$ , as is characteristic of abyssal hills, and are unresolved by conventional global topographic datasets and the general circulation models regularly used to investigate ocean dynamics.

In this article, we exploit the recent advent of several near-global descriptions of topographic roughness on horizontal scales less than  $O(10 \text{ km})$  to assess the impact of small-scale topography on the ocean's dynamical balance. We note that the time-mean internal lee wave drag examined here contains information on the large-scale, time-mean ocean circulation that is distinct and largely independent from the time-mean internal lee wave energy flux computed by Scott et al. (2011) and Nikurashin and Ferrari (2011). This is because, while the instantaneous internal lee wave drag is essentially equivalent to the concurrent internal lee wave energy flux (the energy flux is equal to the drag multiplied by the near-bottom velocity), significant differences between the distributions of the two quantities are introduced by time averaging.<sup>2</sup> Physically, the time-mean internal lee wave energy flux mainly reflects the dissipation of mesoscale eddy flows as they impinge on small-scale topography and generate internal waves, whereas the time-mean internal lee wave drag measures the rate of deceleration of the time-mean ocean circulation associated with the same wave generation process in the presence of a time-mean flow or a skewed eddy field. Thus, if there is no time-mean flow and the eddy field has zero skewness, the time-mean internal lee wave drag must be zero, but the time-mean internal lee wave energy flux may still be large. The two variables become increasingly equivalent as the magnitude of the mean flow substantially exceeds the characteristic amplitude of eddy motions: this is a rare scenario in the ocean, where the kinetic energy of geostrophic eddies is typically greater than that of the time-mean circulation by an order of magnitude (Ferrari and Wunsch 2009).

Our key finding is that, while internal lee wave drag associated with small-scale topography is commonly

<sup>1</sup> Note that since a horizontal stress is a *downward* flux of horizontal momentum the depth-integrated drag force (which we term, rather loosely, the drag in the following) is opposite in sense to the bottom stress.

<sup>2</sup> In contrast to the energy flux, which is a positive-definite scalar with a positive-definite time-mean value, the drag is a signed vector quantity for which time-averaging in the presence of a mesoscale eddy field incurs substantial cancellation. Note, however, that as the drag is nonlinearly dependent on the near-bottom velocity, this cancellation is not perfect in the presence of a mean flow and/or a skewed eddy field.

unimportant in arresting the ocean circulation over much of the globe, it plays a significant role in the dynamics of extensive regions of the ocean (most notably the Southern Ocean). A theoretical perspective on the form drag associated with large- and small-scale topographies is offered in section 2 along with the methodology and data sources underpinning the various terms in the ocean's dynamical balance examined in this article. The results of our calculations are presented in section 3. In section 4, the implications of this work are discussed, and conclusions are drawn.

## 2. Theory, methodology, and data

In this section, we present the methodology and data sources underpinning the four basic terms of the ocean's dynamical balance identified in section 1 [i.e., the source of (angular) momentum or vorticity linked to wind forcing and the sinks associated with form drag by large-scale topography, with form drag by small-scale topography, and with frictional drag at the sea floor] and provide brief theoretical accounts of how the two classes of form drag come about. In section 2a, we report on the estimates of wind stress considered in this work. In section 2b, we derive a theoretical scaling for the dependence of the effectiveness of form drag by large-scale topography on the topographic dimensions, and combine it with observations of the spectral properties of the global sea floor to shed light on the characteristic length scale of form drag seen in general circulation models. We also introduce the form drag calculated in one such model, which is treated as a representative estimate of large-scale topographic form drag throughout the remainder of this study. In section 2c, we outline internal lee wave generation theory and explain how we use it to estimate the form drag by small-scale topography. Finally, the calculation of frictional drag is described in section 2d.

### a. Wind stress

The primary wind stress dataset considered in this work is the European Centre for Medium-Range Weather Forecasts wind stress climatology of Siefridt and Barnier (1993), which forces the Ocean Circulation and Climate Advanced Modeling (OCCAM) project model (see, e.g., Webb et al. 1998) from which an estimate of the large-scale topographic form drag is extracted (see section 2b). The Navy Operational Global Atmospheric Prediction System (NOGAPS) dataset (Rosmond et al. 2002) used in forcing the Hybrid Coordinate Ocean Model (HYCOM) (see, e.g., Scott et al. 2010), the model implicated in the calculation of the small-scale topographic form drag (see section 2c), was also

examined. A high degree of consistency between climatological means of the two wind stress datasets was found, so only the ECMWF climatology is presented in this article.

### b. Form drag by large-scale topography

#### 1) DEPENDENCE OF FORM DRAG ON THE SCALES OF TOPOGRAPHY

As commented on in section 1, the decelerating action of topographic form drag in general circulation models is found to be associated with topographic features typically measuring 500–1000 km across. The dominance of this length scale in the ocean momentum sink in the models may be understood by examining the physical mechanism mediating the setup of cross-topographic pressure gradients for topography of horizontal dimensions greater than  $O(10\text{ km})$ . One example of the setup of topographic form stress by friction is of course the simple barotropic Stommel gyre in a rectangular flat-bottomed ocean. Assuming the wind to be westerly in the northern part of the subtropical basin and decaying to zero at the southern end, then pressure is almost constant along the bounding streamline of flow moving (weakly) southward on the eastern boundary and westward along the southern boundary. However, bottom friction acting on the rapid northward flow in the subtropical western boundary current gives a pressure drop from south to north on the western sidewall. The resultant lower pressure on the western sidewall, compared to that on the eastern sidewall, gives the net westward form drag that balances the eastward wind stress. Although the zonal frictional stress is insignificant, the meridional frictional stress permits the setup of a zonal form drag.

To elicit this point more generally, consider the simple scenario of a quasi-zonal eastward barotropic flow with velocity scale  $U$  on an ocean with depth  $H_2$  impinging on an idealized rectangular plateau-shaped topographic feature (Fig. 1). We assume for simplicity that relative vorticity is unimportant in the potential vorticity budget. This assumption may not always hold, and its validity requires either (i) that the frictional spindown time scale is less than the time scale for fluid to cross topography or (ii) that all length scales (zonal, meridional, and skirt widths) of the topography are much greater than the Rhines scale  $(U/\beta)^{1/2} \sim 100\text{ km}$  for  $U \sim 0.1\text{ m s}^{-1}$ ,  $\beta \sim 1.0 \times 10^{-11}\text{ m}^{-1}\text{ s}^{-1}$ . Over realistic ocean topographic features with scales on the order of the Rhines scale, variation of relative vorticity along streamlines will in fact often lead to substantial additional zonal form drag—Rossby wave drag—as Rossby waves are emitted (McCartney 1975; Gill 1982).

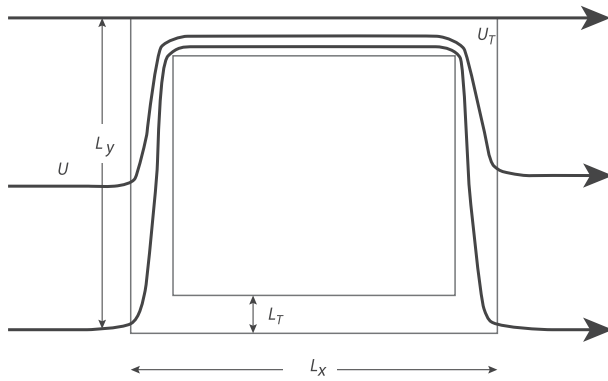


FIG. 1. Plan view schematic of a zonal flow (denoted by the thick lines and arrows) of speed  $U$  impinging on an idealized rectangular plateau (shown by the thin lines) in the Southern Hemisphere. The plateau has zonal length  $L_x$ , meridional width  $L_y$ , and a sloping edge of width  $L_T$ .

The plateau has a height  $\Delta H = H_2 - H_1$ , longitudinal scale  $L_x$ , latitudinal scale  $L_y$ , and “skirts” (sloping areas around the sides) of width  $L_T$  and slope  $S_T = \Delta H/L_T$ . We assume that the plateau is sufficiently high that  $f_N/H_1 < f_S/H_2$  (writing  $f_S$  and  $f_N$  as the Coriolis parameters at the southern and northern ends of the plateau), so flow cannot penetrate onto the plateau. The whole of the upstream flow therefore follows  $f/h$  contours that enter the western skirt of the plateau, thread through the northern skirt (as appropriate to the Southern Hemisphere), and then emerge from the eastern skirt. By continuity, flow speeds along the skirt will thus be on the order of  $U_T = (L_y/L_T)U$ . Of course, this is only an order of magnitude estimate: the flow may not occupy the whole of the skirt (thus giving stronger flow), and flow speed will vary around the plateau.

In the absence of any frictional processes within the boundary currents or change in relative vorticity along geostrophic streamlines, the pressure on an  $f/h$  contour is the same at exit from the eastern skirt as at entry into the western skirt, and there is no net bottom pressure drag against the plateau. However, where there is friction, the pressure will differ from west to east, so the plateau will provide a net drag. Characterizing friction with a quadratic bottom drag  $-c_d \mathbf{u}|\mathbf{u}|$  (where  $c_d$  is a constant drag coefficient), the pressure difference along a streamline entering the skirt a distance  $\alpha L_y$  (where  $0 \leq \alpha \leq 1$ ) south of the northern edge of the plateau from the west and exiting the east will be

$$\Delta p(\alpha) \sim \frac{c_d}{H} U_T^2 (2\alpha L_y + L_x).$$

The total zonal pressure force exerted by the plateau on the ocean is thus

$$\mathcal{P} = \Delta H L_y \int_0^1 \Delta p(\alpha) d\alpha \sim c_d \frac{\Delta H}{H} U_T^2 L_y (L_y + L_x),$$

while the direct zonal frictional drag integrated over the northern skirt is

$$\mathcal{F} = L_T L_x c_d U_T^2.$$

The ratio of the net pressure force to the frictional force is then given as

$$\frac{\mathcal{P}}{\mathcal{F}} = \frac{\Delta H L_y (L_y + L_x)}{H L_T L_x} = \frac{\Delta H L_y (L_y + L_x)}{L_T H L_x}. \quad (2)$$

Expression (2) illustrates how the presence of sloping topography greatly enhances the decelerating action of friction over that of direct frictional drag, by virtue of friction’s role in enabling the setup of a net cross-topographic pressure force. Note that the form drag has no impact on the *energy* budget; it only affects *momentum*. Friction on the other hand has a direct impact on the energy budget, but a lesser (direct) impact on momentum. Equation (2) implies that the net pressure force is relatively most important for plateau-shaped topography whose height  $\Delta H$  is comparable to the depth of the ocean  $H$  and varies over a skirt length scale  $L_T$ , much smaller than the meridional extent of the topography  $L_y$ . For a meridionally elongated ridgelike plateau with  $L_y \gg L_x$ , the zonal frictional force becomes insignificant, but the form drag remains important. Thus, the characteristic horizontal length scale of relatively high, steep and meridionally elongated topographic features present in the ocean should define the size of topography that is most effective at arresting the oceanic flow.

To obtain an estimate of the horizontal dimension characteristic of large-scale topographic form drag, expression (2) must be combined with information on the properties of sea floor topography. To gain such information, we compute a semivariogram (a type of structure function that is widely used in geostatistics) over all ocean depths in excess of 1000 m (Fig. 2a). The semivariogram is defined as

$$\gamma(l) = E[(h(x) - h(x+l))^2]/2, \quad (3)$$

where  $h(x)$  is the topography at position  $x$ ,  $l$  is the lag distance (here restricting to a one-dimensional function), and  $E[ ]$  is the expectation operator. The semivariogram is estimated by averaging the square of differences as a function of lag distance and dividing by 2. The global semivariogram is well matched by a von Kármán model (Goff and Jordan 1988):

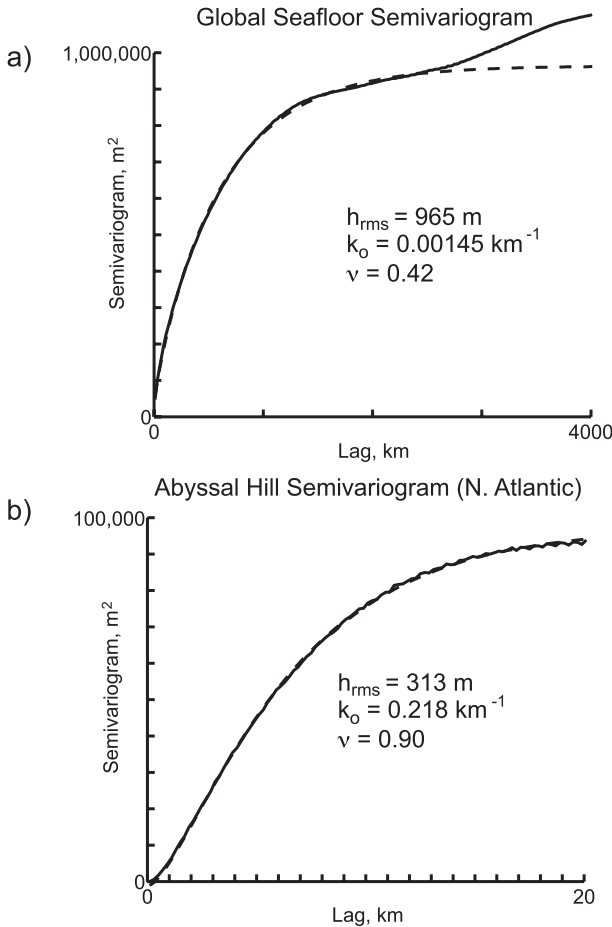


FIG. 2. Semivariograms computed from (a) global topography (Smith and Sandwell 2004) and (b) multibeam bathymetry data from the flanks of the northern Mid-Atlantic Ridge (Goff et al. 1995) (solid lines). The global semivariogram was limited to depths in excess of 1000 m and latitudes in the range from 75°S to 75°N. Dashed lines indicate the best-fit von Kármán model, with parameters as shown, estimated by least squares fit.

$$\gamma_{vK}(l) \equiv h_{rms}^2 \left[ 1 - \frac{G_\nu(k_0 l)}{G_\nu(0)} \right], \quad (4)$$

where

$$G_\nu(r) = r^\nu K_\nu(r), \quad 0 \leq r < \infty, \quad \nu \in [0, 1]. \quad (5)$$

Here  $K_\nu$  is the modified Bessel function of the second kind of order  $\nu$ . The von Kármán model is a band-limited fractal with self-affine scaling at wavenumbers much less than  $k_0$  and a flat spectrum at wavenumbers much greater than  $k_0$ . The parameter  $h_{rms}$  is the rms height variability, and  $\nu$  is the Hurst number, from which the fractal dimension can be determined as  $D = 3 - \nu$  for a surface. At  $\nu = 0.5$ , the von Kármán model is identical to an exponential form. Best-fit model parameters to the

global semivariogram (Fig. 2a) are  $h_{rms} = 965$  m,  $k_0 = 0.00145$  km<sup>-1</sup>, and  $\nu = 0.42$  ( $D = 2.58$ ).

The global semivariogram model (Fig. 2a) demonstrates that sea floor features increase in a self-affine manner up to horizontal scales of  $\sim 1000$  km; 80% of the semivariance is contained in features smaller than this scale. Above this scale, sea floor features do not appreciably increase in height as their lateral scale increases. The upper limit of the self-affine regime can be thought of as a “characteristic scale” of the topography (Goff and Jordan 1988). If we assume that, in the self-affine regime, the skirt length  $L_T$  is approximately a constant proportion of “feature length” ( $L_x$  and  $L_y$ ), then Eq. (2), in the absence of knowledge of the ratio  $L_y/L_x$ , reduces to a dependence on  $\Delta H/H$ ; that is, the net pressure force increases with increasing feature height. At larger scales, however,  $L_x$  and  $L_y$  increase while  $\Delta H/H$  does not. Because slopes are decreasing rapidly with increasing scale in this regime, it is reasonable to assume that  $L_T$  will increase as a proportion of  $L_x$  and  $L_y$ , thereby decreasing net pressure force with increasing scale. Although this argument depends on overly simplistic generalities, it nevertheless provides a reasonable expectation for a peak in influence on oceanic drag related to the characteristic horizontal scale of the seafloor of  $\sim 1000$  km. This interpretation is consistent with the aforementioned finding that topography of the same approximate scale dominates the ocean momentum sink in general circulation models.

## 2) ESTIMATE OF LARGE-SCALE TOPOGRAPHIC FORM DRAG

The estimate of form drag by large-scale topography examined here is taken from the work of Hughes and de Cuevas (2001). The estimate is based on fields from the 1/4°-resolution OCCAM model and is quantitatively similar to diagnostics from other general circulation models of coarse or eddy-permitting resolution (e.g., Lu and Stammer 2004; Eden and Olbers 2009). See Hughes and de Cuevas (2001) for details of the calculation procedure.

### c. Form drag by small-scale topography

#### 1) INTERNAL LEE WAVE GENERATION THEORY AND CALCULATION PROCEDURE

The generation of internal lee waves by geostrophic flow over topography has been studied from a theoretical perspective by Bell (1975) and Gill (1982), amongst others. Adopting the traditional approximation of ignoring the horizontal components of the Coriolis force, the linearized density equation and nonhydrostatic, vertical momentum equation provide a relation between

pressure and vertical velocity. For small-amplitude sinusoidal topography the vertical velocity is imposed by the kinematic boundary condition, and one can solve for the vertical flux of horizontal momentum resulting from the pressure–topographic slope correlation. The momentum flux is nonzero if the oscillations generated by flow over topography can propagate as waves, that is, if their intrinsic frequency  $\sigma = \mathbf{k} \cdot \mathbf{u}$  [where  $\mathbf{k} = (k, l)$  is the horizontal wavenumber of the topography and  $\mathbf{u} = (u, v)$  is the near-bottom horizontal velocity] lies between the inertial ( $f$ ) and buoyancy ( $N$ ) frequencies,  $|f| < |\sigma| < N$ . The horizontal momentum extracted from the background flow is carried upward by the waves as they radiate away from the boundary and is deposited when the waves break, thereby exerting a drag on the background flow. Throughout this work, we will assume that the internal lee waves generated by geostrophic flow over topography do not experience significant horizontal propagation (relative to the horizontal spacing of the calculation grid) and that they break at some level within the water column, such that the depth-integrated internal wave drag matches the vertical flux

$$-\tau_{\text{iw}}^{\text{lin}}(x, y, t) = \frac{\rho_0}{4\pi^2} \int_{-\infty}^{\infty} \int_{-\infty}^{\infty} S(\sigma) \frac{\mathbf{k}}{\sqrt{k^2 + l^2}} P(k, l) \sqrt{N^2 - \sigma^2} \sqrt{\sigma^2 - f^2} dk dl, \quad (6)$$

where  $\rho_0$  is the fluid density and

$$S(\sigma) = \begin{cases} 1 & \text{if } |f| < |\sigma| < N; \sigma > 0, \\ -1 & \text{if } |f| < |\sigma| < N; \sigma < 0, \\ 0 & \text{otherwise.} \end{cases}$$

Generally, abyssal  $N$  varies little on time scales of up to decades, so  $N = N(x, y)$  will be approximated with climatological values. In contrast,  $\sigma = \sigma(x, y, t)$  varies significantly in space and time because of the time dependence of the background flow. It will be assumed that the flow is quasi-steady on time scales longer than the inertial period, although forcing by near-inertial flows could be an additional contribution to generation not accounted for in this study (Kasahara 2010).

Note that the internal lee wave drag is not necessarily aligned with the near-bottom flow. For instance, the trivial case with monochromatic topography with wavenumber  $\mathbf{k}_0$  gives from (6) a drag in the  $\mathbf{k}_0$  direction. This makes physical sense, as the flow parallel to such monochromatic topography does not interact with it; only the flow *across* topography generates waves. In fact, oceanic topographies are generally sufficiently nonisotropic that the internal wave drag is generally closely aligned to the normal direction of the topography (see the detailed

of horizontal momentum associated with the waves at generation. The first assumption follows from the intrinsic role that the geostrophic flow plays in the generation and persistence of the internal lee waves, which locks them to the horizontal proximity of their generation site (e.g., Nikurashin and Ferrari 2010a). The second reflects our present lack of knowledge on the characteristic evolution of internal lee waves as they propagate vertically, and the high likelihood of eventual breaking, particularly in the presence of nonlinearity in the internal wave field and buoyancy scaling effects (see Naveira Garabato et al. 2004; Nikurashin and Ferrari 2010a for a discussion). Note, though, that, if the dissipation of the internal lee waves within the water column is not complete, the wave drag will be reduced proportionally.

Representing the topography by a two-dimensional power spectrum  $P(k, l; x, y)$  that varies slowly on spatial scales much larger than the wavelengths of internal lee waves, it may be shown that the net topographic form drag resulting from the sum of all contributions within the internal wave band is given by

discussion in section 1c of appendix B and Fig. B4). Of course, only the component of the velocity parallel to the wave drag contributes to the energy transfer  $\tau_{\text{iw}} \cdot \mathbf{u}$  into the internal wave field discussed in Scott et al. (2011).

The linear theory above describes well the generation of internal lee waves when  $N \gg |f|$  so that the traditional approximation applies and when the topography has small amplitude in the sense of

$$\frac{1}{\text{Fr}} \equiv \frac{HN}{U} \leq \frac{1}{\text{Fr}_c}, \quad (7)$$

where  $\text{Fr}$  is the Froude number of the flow,  $U$  is a background velocity scale,  $H$  is the amplitude of the topographic variations, and  $\text{Fr}_c$  is a critical Froude number. As topographic amplitude and buoyancy frequency increase or as background velocity decreases, the flow becomes increasingly blocked by the topography leading to substantially less form drag than given by (6). Empirical corrections for this phenomenon have been put forward and tested with laboratory experiments and numerical simulations. These are reviewed by Scott et al. (2011) and will not be discussed here. We follow those authors in adopting a correction for topographic blocking of the form

$$\tau_{iw} = \tau_{iw}^{lin} G = \tau_{iw}^{lin} \frac{L}{\pi} \left[ \arccos(1-2L) - 2(1-2L)\sqrt{L(1-L)} \right], \tag{8}$$

where

$$L = \begin{cases} 1 & \text{if } Fr^{-1} \leq Fr_c^{-1}, \\ \frac{Fr}{Fr_c} & \text{if } Fr^{-1} > Fr_c^{-1}. \end{cases}$$

Our results are insensitive (to better than 1%) to the choice of other possible corrections (Scott et al. 2011).

As in Scott et al.,  $Fr_c^{-1}$  is taken as 0.7, and the amplitude of the topography in (7) is defined as

$$H^2 = \frac{1}{4\pi^2} \int_{-\infty}^{\infty} \int_{-\infty}^{\infty} |S(\sigma)| P(k, l) dk dl. \tag{9}$$

This is a metric of the amplitude of the topographic variations contributing to the generation of internal lee waves and is therefore time-dependent (through  $\sigma$ ).

Note that, despite the recent convergence between different corrections for blocking effects in the literature [including (8)], this expression is unlikely to be definitive and may be associated with substantial uncertainty. The clearest illustration of this point is provided by the poorly known extent to which (8) and other equivalent corrections adequately capture the form drag associated with highly nonlinear high-drag states, occurring for  $Fr^{-1}$  values of  $O(1)$  (e.g., Eckermann et al. 2010). Such high-drag states are characterized by hydraulic jumps, intense internal wave breaking, and vortex shedding at and around topographic obstacles, and may be largely described in terms of internal wave dynamics (Peltier and Clark 1979; Bacmeister and Pierrehumbert 1988; Welch et al. 2001). Their effective drag has been found to exceed linear theory predictions by  $O(10\%–100\%)$ , depending on various aspects of topographic configuration (Welch et al. 2001; Wells et al. 2008; Eckermann et al. 2010). Expression (8) may thus provide a lower-bound estimate of  $|\tau_{iw}|$  for  $Fr^{-1} \sim 1$ . Nonetheless, since such high  $Fr^{-1}$  values occur only rarely in the ocean (specifically, in less than 10% of all the spatiotemporal points in our calculation; see Scott et al. 2011), this and other blocking-related issues are unlikely to have a major impact on our results.

Numerical integration of (6) is performed using  $100 \times 100$  grid points separately over each quadrant in  $(k, l)$  space. Wavenumber points increase geometrically in magnitude, from  $k_{min} = l_{min} = 10^{-6} \text{ rad m}^{-1}$  to  $k_{max} = l_{max} = 0.1 \text{ rad m}^{-1}$ ; this provides adequate numerical convergence. To produce a global map of the climatological

(time-mean) value of the topographic form drag associated with internal lee wave generation,  $-\overline{\tau_{iw}}(x, y, t)$  (where the overbar indicates an average over many mesoscale eddy periods), knowledge of the spatial distribution of the topographic power spectrum  $P(k, l)$ , the buoyancy frequency  $N$ , and the time-varying geostrophic flow near the ocean floor,  $\mathbf{u}$ , is required throughout the global ocean. The sources of these data are detailed in the following subsections.

## 2) SMALL-SCALE TOPOGRAPHY

In order for small-scale topography to exert a drag on ocean circulation, internal lee wave generation (and, ultimately, breaking) must occur. The precise horizontal scales of the topography exerting a drag at any one location and time can therefore be determined from the condition for internal lee wave generation:  $|f| < |\sigma| = |\mathbf{k} \cdot \mathbf{u}| < N$ . Substituting characteristic values of  $|f| \sim 1^{-4} \text{ rad s}^{-1}$ ,  $N \sim 10^{-3} \text{ rad s}^{-1}$  and near-bottom background velocities  $|\mathbf{u}|$  in the range  $0.01 \text{ m s}^{-1}$  to  $0.1 \text{ m s}^{-1}$ , it may be inferred that the topographic features implicated in internal lee wave generation have horizontal wavelengths of 100 m to 10 km. At these small scales, abyssal hills are the most prominent feature of the topographic fabric of the ocean floor and prevail over larger-scale features such as spreading ridges, fracture zones, and seamounts. They are created at midocean ridge spreading centers by faulting and volcanism, and are modified in time by sedimentation. They exhibit characteristic scales from 50 to 300 m in height, 2 to 8 km in width, and 10 to 25 km in length and obey fractal scaling below a corner wavenumber (Goff and Jordan 1988, 1989; Goff et al. 1997); see Fig. 2b. Utilizing the two-dimensional anisotropic spectral form of the von Kármán model, these authors put forward a representation of small-scale topography by a power spectrum of the form

$$P(k, l) = 4\pi\nu \frac{h_{rms}^2}{k_n k_s} \left[ \frac{|\mathbf{k}|^2}{k_s^2} \cos^2(\theta - \theta_s) + \frac{|\mathbf{k}|^2}{k_n^2} \sin^2(\theta - \theta_s) + 1 \right]^{-(\nu+1)}, \tag{10}$$

where  $k_s$  and  $k_n$  are the wavenumbers in the strike and normal directions, respectively, with  $k_n \geq k_s$ ;  $\theta_s$  measures the angle clockwise from true north to the strike direction;  $\theta = \arctan(k/l)$  is the angle clockwise from true north of the wavenumber vector; the Hurst number  $\nu$  indicates the steepness of the spectrum at high wavenumbers; and  $h_{rms}$  is the rms topographic height variability, defined such that

$$h_{\text{rms}}^2 = \frac{1}{4\pi^2} \int_{-\infty}^{\infty} \int_{-\infty}^{\infty} P(k, l) dk dl.$$

In subsequent analysis, the set of parameters ( $h_{\text{rms}}$ ,  $k_s$ ,  $k_n$ ,  $\nu$ ,  $\theta_s$ ) is used to characterize the small-scale topography.

A major difficulty in understanding the role of small-scale topography in arresting the ocean circulation is that abyssal hill scales cannot be resolved by conventional global topographic datasets, which are largely reliant on satellite altimetric gravity measurements and have a characteristic horizontal resolution of 10–20 km (e.g., Smith and Sandwell 2004). In the present work, we take advantage of the recent development of two quasi-independent, near-global datasets of small-scale topographic parameters by Goff and Arbic (2010) and Goff (2010) (respectively referred to as GA2010 and G2010 hereafter) verified by comparison with available multi-beam bathymetric observations. The GA2010 dataset predicts abyssal hill roughness statistical parameters via relationships for the average statistical properties of abyssal hills as a function of spreading rate and direction, and for the modification to these roughness parameters as a function of sediment thickness. The G2010 dataset is derived by relating the small-scale variability in satellite altimetric gravity measurements to the statistical properties of the abyssal hill morphology using the upward continuation formulation. Details of the construction of the two datasets may be found in GA2010 and G2010. Further discussion of how the datasets compare is provided by Scott et al. (2011). While the two datasets are found to compare well in most respects, here we draw on the conclusions of those authors and make use of the slightly superior G2010 dataset for our default calculation, while considering the GA2010 in sensitivity tests (appendix A). Our treatment of the two datasets for computational purposes is identical to that by Scott et al. (2011), and we refer the reader to that article for a description of those methodological details. Here  $h_{\text{rms}}$  is found to be the most important topographic parameter in shaping the spatial patterns of internal lee wave generation. Its distribution for the G2010 dataset is mapped in Fig. 3a. Enhanced abyssal hill roughness is seen primarily in the slow-spreading midocean ridges of the Atlantic and Indian basins, their extensions into the Southern Ocean, and the Pacific–Antarctic Ridge.

### 3) NEAR-BOTTOM BUOYANCY FREQUENCY

Our estimate of the near-bottom stratification is based on the *World Ocean Atlas 2009* (WOA2009) seasonal temperature and salinity climatology (Locarnini et al. 2006; Antonov et al. 2006). Details of the calculation,

gridding, and validation procedures are given in Scott et al. (2011). The resulting distribution of abyssal  $N$  is shown in Fig. 3b. Near-bottom  $N$  values span a range of approximately an order of magnitude. They are dependent primarily on ocean depth, with an increase (decrease) in  $N$  in relatively shallow (deep) water. Water mass age is also seen to have an imprint in the distribution of near-bottom stratification, with, for example, low  $N$  values across the old waters of the North Pacific.

### 4) NEAR-BOTTOM GEOSTROPHIC FLOW

The statistics of the near-bottom geostrophic flow are estimated using a specific run of the global  $1/12^\circ$  Hybrid Coordinate Ocean Model (HYCOM) conducted at the Naval Research Laboratory, Stennis Space Center. The run in question (hereafter DA) assimilates available satellite altimetric and sea surface temperature measurements and a collection of hydrographic observations from various sources. Further details of the DA run and references on the model are given by Scott et al. (2010, 2011). The former set of authors assessed the realism of the kinetic energy of the DA run and a companion free-running HYCOM simulation along with two other global-eddy ocean general circulation models by reference to over 5000 moored current meter records scattered around the globe. They found the DA (free running) run to overestimate (underestimate) near-bottom kinetic energy by a factor of 1.3 (3). Thus, we will consider the DA run to be our best estimate of the near-bottom geostrophic flow. Following Scott et al. (2011), we will analyze 360 days of data and use 5-day averages of the model flow field in our calculations to filter out high-frequency ageostrophic signals. Like those authors, we will take the velocity on the second deepest vertical level (level 2) at each location of the HYCOM ocean as our best estimate of the near-bottom flow, for this is the deepest model level outside of the frictional bottom boundary layer. However, we will consider the data at the deepest and third deepest levels (levels 1 and 3, respectively) in sensitivity tests (appendix A). See Scott et al. (2011) for a more detailed description of our HYCOM data processing procedure.

The time-mean velocity and kinetic energy on level 2 of the DA run for year 2006 (used in our default calculation) are displayed in Figs. 3c and 3d, respectively. It is shown in section 4 that, over a range of conditions that hold widely in the ocean,  $|\tau_{\text{iw}}|$  scales approximately with  $|\mathbf{u}|$  elevated to a power in the range of 1 to 2 for reasonable values of  $\nu$ , such that both the time-mean velocity and kinetic energy are valuable descriptors of the forcing flow. The two variables have many broad similarities. Although kinetic energy reflects primarily

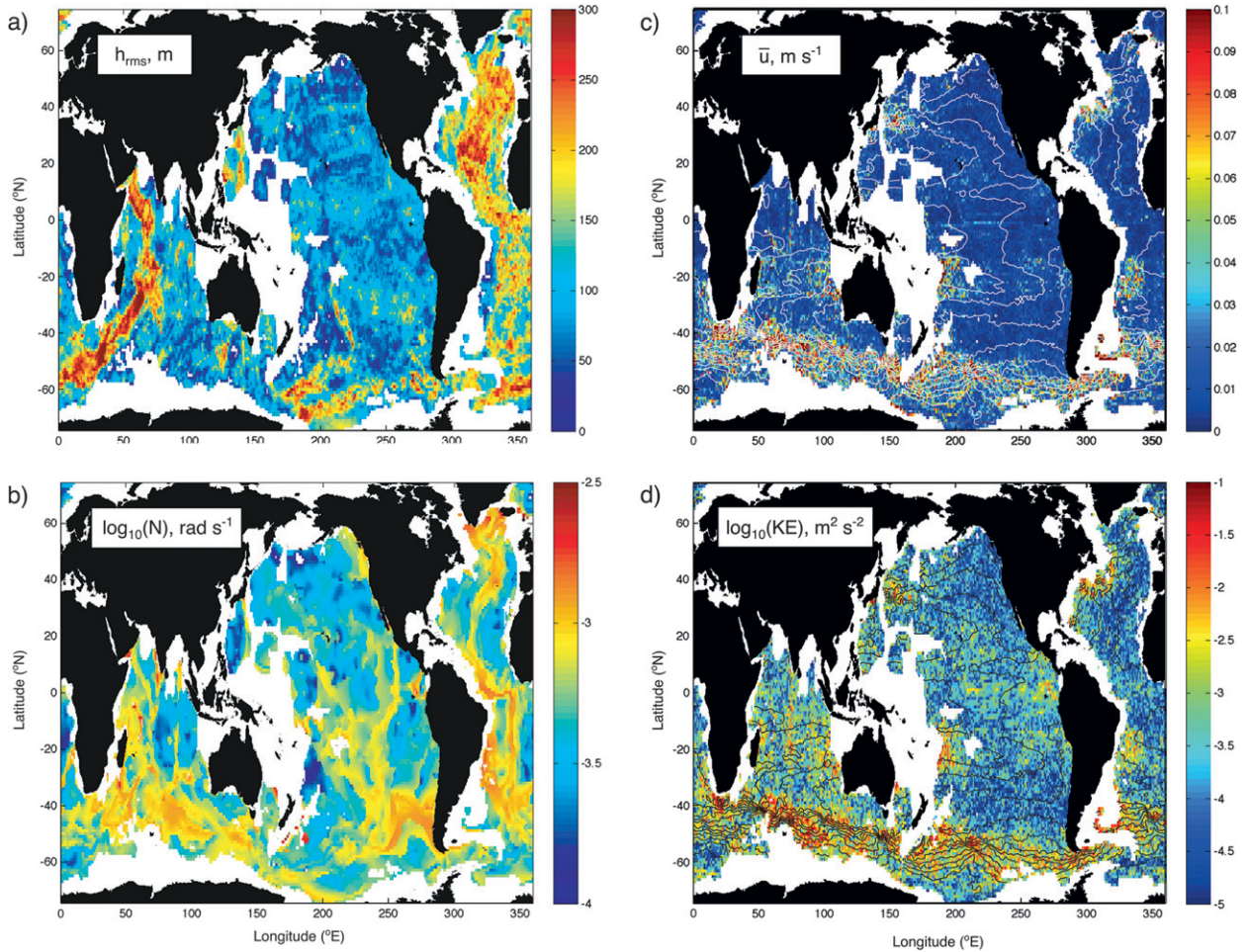


FIG. 3. Maps of (a) small-scale bottom roughness from G2010, (b) near-bottom buoyancy frequency from *WOA2009*, (c) time-mean (for 2006) near-bottom (second grid above bottom) speed from HYCOM DA, and (d) near-bottom kinetic energy from the same period in HYCOM DA. White contours in (c), black in (d), indicate time-mean sea surface height in the model (contour interval 0.2 m).

mesoscale eddy variability rather than the time-mean flow, the two are inextricably linked through dynamical (mainly baroclinic) instability processes (e.g., Smith 2007). It is thus no surprise that both variables indicate energetic flows in the same regions, most obviously in the Antarctic Circumpolar Current (ACC) in the Southern Ocean and the western boundary currents of the three major ocean basins. Note, however, that the mean velocity has a more filamented structure than the kinetic energy. This reflects the contrast between the jetlike nature of mean ocean flows and the smearing out of such mean filamentary structures by mesoscale eddy variability.

#### d. Frictional drag

The frictional drag is calculated from the HYCOM DA velocity field at the deepest grid point in each location in the model ocean (i.e., in the set of grid points

embedded in the frictional bottom boundary layer in the model). The calculation is conducted using a quadratic formulation of the frictional drag,

$$-\tau_b(x, y, t) = -\rho_0 c_d |\mathbf{u}_b| \mathbf{u}_b. \quad (11)$$

Here  $c_d$  is the frictional drag coefficient, set to 0.0022 as in HYCOM (which contains quadratic frictional drag), and  $\mathbf{u}_b$  is the velocity vector within the frictional boundary layer.

### 3. Results

To assess the role of small-scale topography on the ocean's dynamical balance, in this section we examine the significance of internal wave drag in the context of other source and sink terms in the oceanic budgets of momentum, angular momentum, and vorticity. Only

time-mean (in the sense of an average over many mesoscale eddy periods) quantities are considered here, as pertains to the dynamics of the time-mean ocean circulation.

Figure 4 shows estimated spatial distributions of the source (wind stress  $\overline{\tau_w}$ ) and two sinks (internal wave drag  $-\overline{\tau_{iw}}$  and frictional drag  $-\overline{\tau_b}$ ) of the ocean's momentum. The other sink (form drag by large-scale topography) is not shown because displaying it in this manner (without first having integrated spatially across large-scale topographic features) would simply reveal very large numbers of alternating sign associated with reversing topographic slopes and would thus be uninformative.

It is readily seen that both internal wave drag (Fig. 4b) and frictional drag (Fig. 4c) account for a relatively minor fraction of the local wind stress (Fig. 4a) over large areas of the global ocean. There are, however, a number of important exceptions. The most obvious of these is the ACC in which the combination of strong near-bottom flows (Figs. 3a,b) and sizeable small-scale topographic roughness (Fig. 3d) leads to  $\overline{\tau_{iw}}$  values that are commonly in the range from 0.03 to 0.08  $\text{N m}^{-2}$ , or approximately 10%–50% of the local wind stress. Internal wave drag is also a significant momentum sink in several regions of rough small-scale topography in the equatorial and Southern Hemisphere oceans, most notably over the axial ridge systems of the Indian and Atlantic basins.

As highlighted in section 1, the internal wave drag is nonlinearly dependent on the near-bottom velocity, such that the time-mean internal wave drag is nonzero in the presence of a skewed mesoscale eddy field as well as of a time-mean flow. The relative contributions of time-mean and eddy flows to the time-mean internal wave drag are quantified in Fig. 5. This illustrates that the time-mean internal wave drag associated with the time-mean flow (Fig. 5a) and that associated with eddy effects (Fig. 5b) have similar spatial distributions to, and account for, comparable fractions of the total time-mean wave drag. The latter finding is brought out most clearly in Fig. 5c, which shows that the contribution from the time-mean flow characteristically exceeds that from eddy effects by a little less than a factor of 2.

It was noted in section 2c.1 that the presence of two-dimensional topography may cause the internal wave drag to be misaligned with the near-bottom flow. In fact (see appendix B section 1c and Fig. B4) for typically anisotropic topography, the internal wave drag is approximately aligned along the normal orientation of the topography, that is, perpendicular to the strike, whatever the orientation of the bottom flow. This effect is quantified in Fig. 6, which shows the probability density

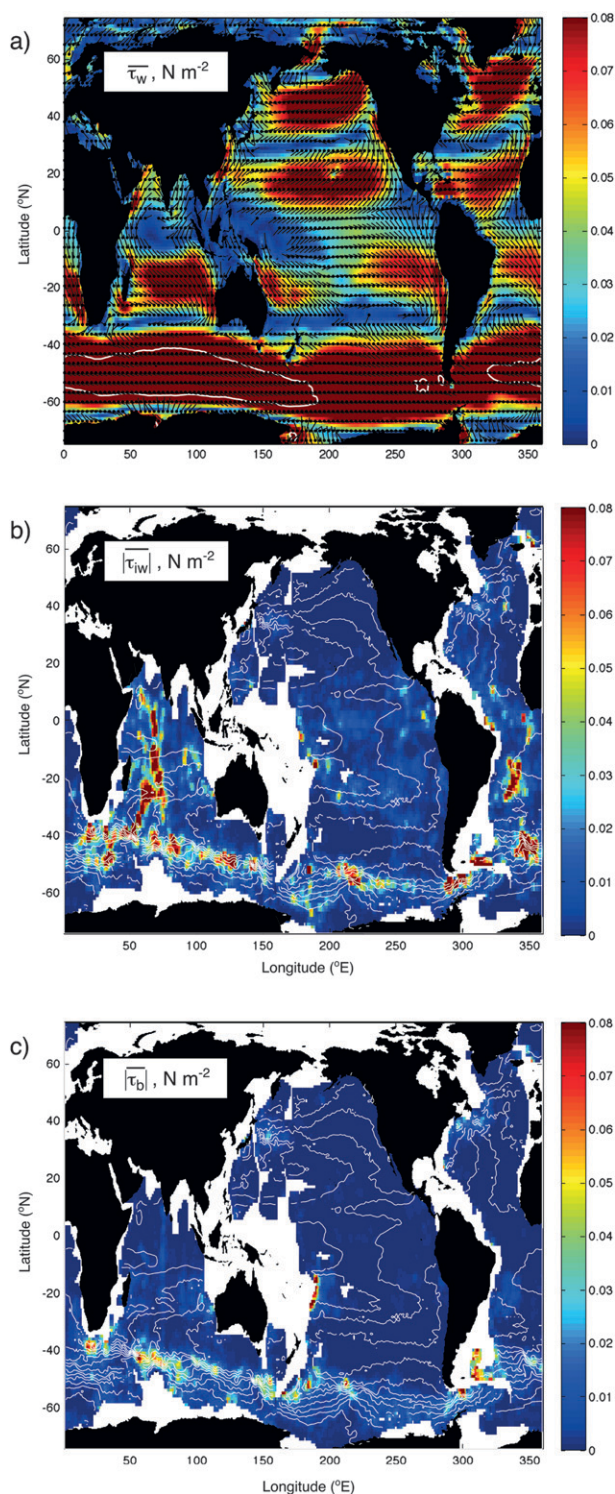


FIG. 4. Maps of time-mean terms in the ocean's momentum balance: (a) climatological wind stress from OCCAM; (b) internal wave drag from the default calculation; and (c) frictional drag from the default calculation. White contours in (b),(c) indicate time-mean sea surface height in the model (contour interval 0.2 m). The topographic form drag associated with large-scale topography is not shown for the reasons stated in section 3.

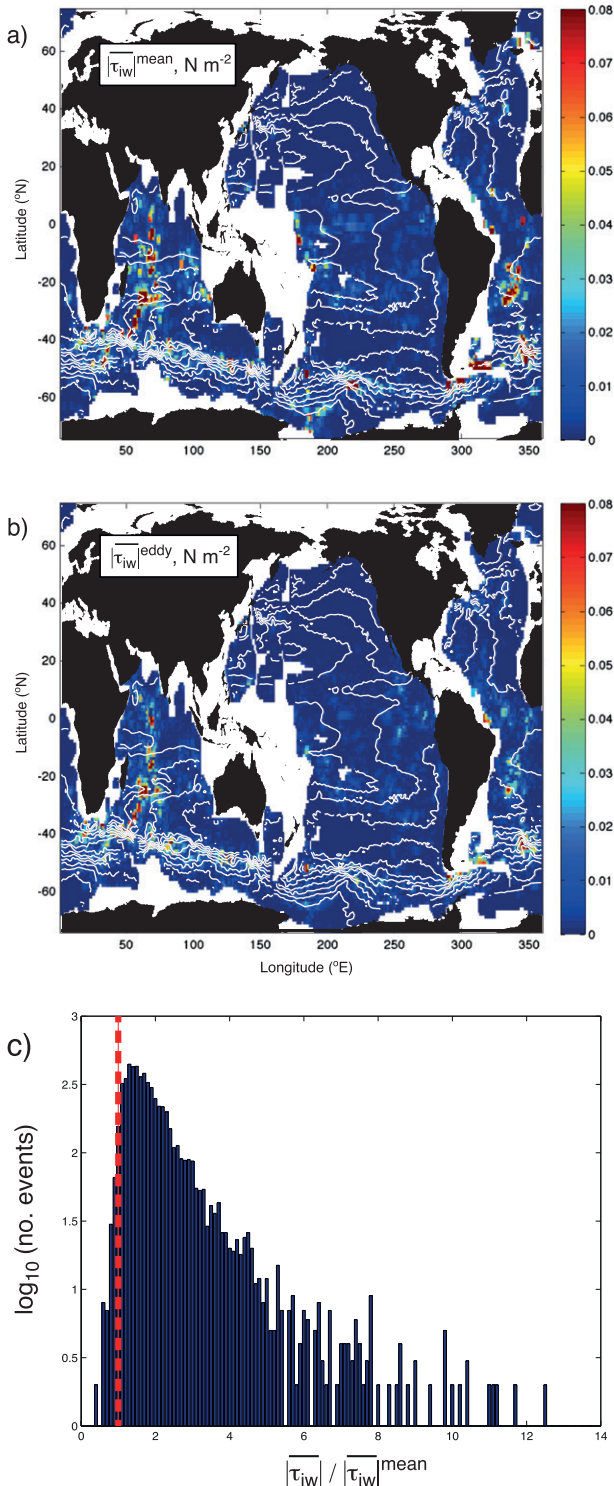


FIG. 5. Maps of the contributions to the time-mean internal wave drag (Fig. 4b) from (a) the time-mean flow and (b) eddy effects. White contours indicate time-mean sea surface height in the model (contour interval 0.2 m). (c) Histogram of the ratio between the time-mean internal wave drag and the contribution from the time-mean flow. The red dashed line indicates a ratio of 1.

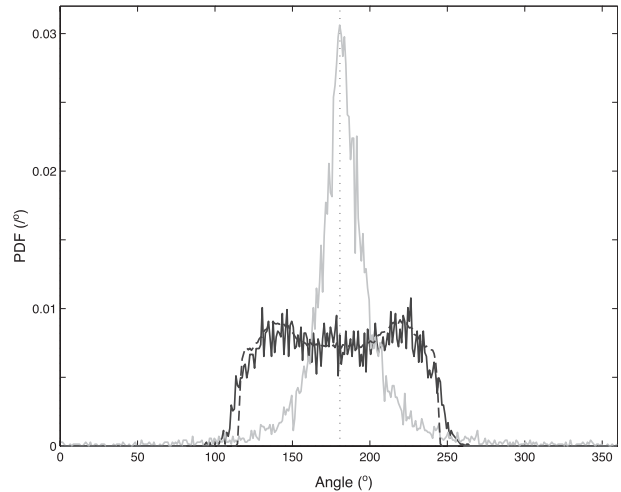


FIG. 6. Probability density functions (pdfs) of the angle between the annual-mean internal wave drag and near-bottom velocity from the default calculation (solid black line), the instantaneous internal wave drag and near-bottom velocity from the same calculation (dashed black line), and the annual-mean frictional drag and bottom velocity (gray line).

function of the angle between the internal wave drag and the near-bottom flow for both instantaneous (dashed black line) and time-mean (solid black line) versions of those variables. In both cases, internal wave drag is directed broadly, but not exactly, in opposition to the near-bottom velocity vector. The function denotes a plateau-shaped distribution: angles of  $\pm 60^\circ$  around  $180^\circ$  have an approximately equal likelihood of occurrence, whereas significantly greater angles occur much less frequently. The rms deviation of  $-\tau_{iw}$  ( $-\overline{\tau_{iw}}$ ) from exact misalignment (i.e., a  $180^\circ$  difference in direction) with  $\mathbf{u}$  ( $\overline{\mathbf{u}}$ ) is  $36.9^\circ$  ( $3.85^\circ$ ).

Frictional drag is generally a less significant momentum sink than internal wave drag by a factor of 2–4. It is enhanced in the ACC (though often in different regions to those of strong internal wave drag) and, to a lesser extent, in western boundary currents. Its alignment at  $180^\circ$  to the (time-mean) near-bottom velocity vector is much closer than for the internal wave case, with the great majority of calculation grid points exhibiting angles between  $-\overline{\tau_b}$  and  $\overline{\mathbf{u}_b}$  that are within  $20^\circ$  of that direction (see gray line in Fig. 6). Naturally, the probability density function of the angle between the instantaneous frictional drag,  $-\tau_b$ , and near-bottom velocity,  $\mathbf{u}_b$ , is  $180^\circ$  by definition [Eq. (11)].

The prevalence of internal wave drag over frictional drag and the regional significance of the former are also apparent in the ocean’s angular momentum balance. The four terms of this balance (i.e., the angular momentum sources and sinks contributed by the zonal

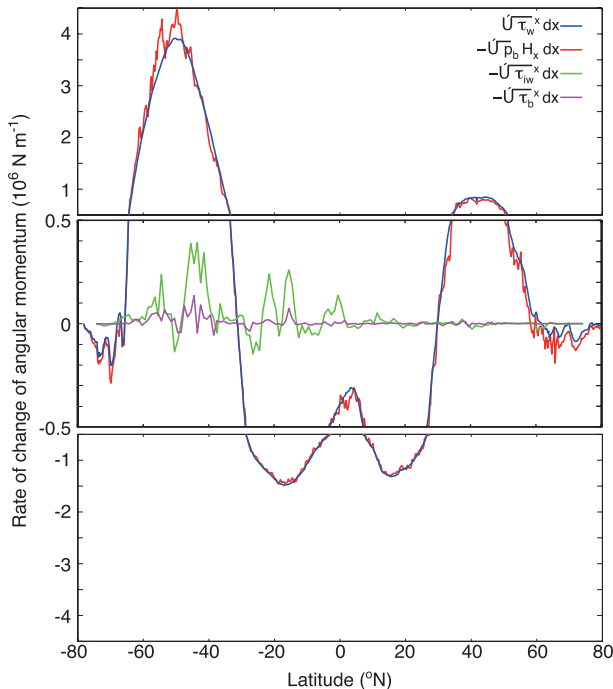


FIG. 7. Zonally integrated terms in the ocean's angular momentum balance: climatological wind stress contribution from OCCAM, large-scale topographic form drag term from OCCAM, internal wave drag term from the default calculation, and frictional drag term from the default calculation.

components of the wind stress, the large-scale topographic form drag, the internal wave drag, and the frictional drag) are shown in Fig. 7. In OCCAM, the bulk of the angular momentum input by the wind stress is balanced by the large-scale topographic form drag term. Both are characterized by values of  $O(10^6) \text{ N m}^{-1}$ . The frictional drag contribution is, as in our estimate, smaller than the dominant terms by at least an order of magnitude. Internal wave drag, however, changes the ocean's angular momentum at a rate that is typically several times that of the frictional drag and peaks at magnitudes of  $\sim 4 \times 10^{-7} \text{ N m}^{-1}$ , approximately 10% of the global peak in the wind stress term. Thus, despite the occurrence of considerable cancellation between internal wave stresses of opposite sign in the zonal integral, internal wave drag provides a significant contribution to the ocean's angular momentum budget, primarily in the Southern Hemisphere.

An alternative perspective of the role of internal wave drag in the ocean's dynamical balance is provided by Fig. 8, which illustrates the distributions of the sources and sinks of oceanic vorticity. These are the wind stress curl ( $\nabla \times \overline{\tau}_w$ ), the large-scale bottom pressure torque ( $\nabla \overline{p}_b \times \nabla H$ ), the small-scale bottom pressure torque associated with internal wave drag ( $-\nabla \times \overline{\tau}_{iw}$ ), and the

frictional torque ( $-\nabla \times \overline{\tau}_b$ ). The driving of the ocean circulation by the wind is apparent in Fig. 8a. The wind inputs vorticity to the ocean with the sign characteristic of the general circulation at a rate of  $O(10^{-7}) \text{ N m}^{-3}$ . Thus, input of positive vorticity to the ocean takes place over the subpolar gyres and equatorial region of the Northern Hemisphere, the subtropical gyres of the Southern Hemisphere, and the northern flank of the ACC; negative vorticity is sourced to the ocean in the subtropical gyres of the Northern Hemisphere, the equatorial region of the Southern Hemisphere, and the southern flank of the ACC. The arresting action of large-scale topography can be appreciated in Fig. 8b. North of the Southern Ocean, this takes the form of a series of pairs of quasi-meridional bands of oppositely signed bottom pressure torque near western boundaries and certain midocean topographic features. The sign of the bands indicates that topography is generally a source of cyclonic (anticyclonic) vorticity in the anticyclonic (cyclonic) flanks of boundary flows, and thereby decelerates those flows. In the Southern Ocean, the arrest of the ACC by large-scale topography stands out as two quasi-zonal bands of positive (to the south) and negative (to the north) bottom pressure torque. Broadly speaking, the characteristic magnitude of the large-scale bottom pressure torque is comparable to that of the wind stress across much of the global ocean.

The opposite is true of the small-scale bottom pressure torque associated with internal wave drag (Fig. 8c), which represents a minor contribution ( $\ll 10^{-7} \text{ N m}^{-3}$ ) to the depth-integrated vorticity balance over large areas of the ocean. Nonetheless, the same important exceptions mentioned in the preceding discussion of the momentum balance are readily noted, that is, the ACC and several regions of rough small-scale topography in the equatorial and Southern Hemisphere oceans. There, bottom pressure torques of  $O(10^{-7}) \text{ N m}^{-3}$  (comparable to the wind stress curl) are widespread, indicating that internal wave drag leads to a significant deceleration of the ocean circulation. In several subtropical regions of the Indian and South Atlantic Oceans, small-scale topography appears to contribute at least as much as large-scale topography to the arrest of the flow. In the ACC, the large-scale term is generally dominant, but the internal wave contribution commonly amounts to 10%–30% of the large-scale bottom pressure torque. Finally, the contribution of frictional drag to the depth-integrated vorticity balance is illustrated by Fig. 8d. The frictional torque is small compared to the other terms. The only noticeable frictional contribution is seen in the ACC, but even there the frictional term is smaller than the internal wave term, typically by a factor of 2–3.

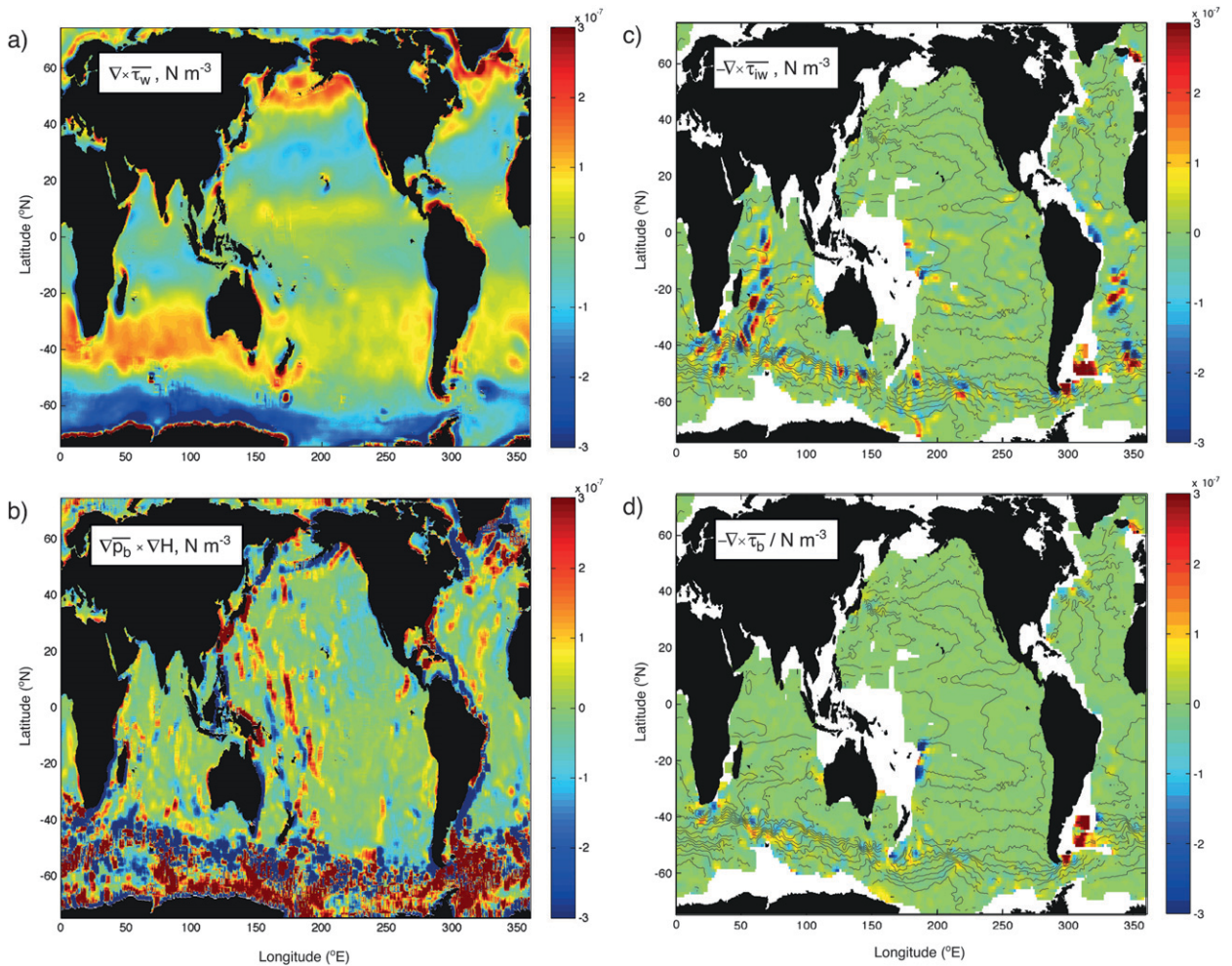


FIG. 8. Maps of time-mean terms in the ocean's vorticity balance: (a) climatological wind stress curl from OCCAM, (b) large-scale bottom pressure torque, (c) internal wave torque from the default calculation, and (d) frictional torque from the default calculation. The black contours in (c),(d) indicate time-mean sea surface height in HYCOM DA (contour interval 0.2 m).

To conclude, we note that the quantitative description of the impact of internal wave drag on the ocean's dynamical balance presented in this section is robust to a range of plausible changes in the calculation's input parameters. This is demonstrated by the sensitivity tests outlined in appendix A, which show that our estimate of the contributions of internal wave drag to the ocean's depth-integrated (angular) momentum and vorticity budgets is most sensitive to the choice of near-bottom velocity field. Varying the HYCOM vertical level at which the near-bottom velocity is extracted from the default value (2) to 1 or 3, or changing the simulation year used in the calculation, leads to relatively modest changes in the magnitude of internal wave drag terms of approximately 10%–25%, with no significant variation in spatial patterns. Changes in other input parameters (including the small-scale topographic dataset) induce

variations in the amplitude of internal wave drag terms of  $\sim 10\%$  at most.

#### 4. Discussion and conclusions

The results of the preceding analysis suggest that, while internal wave drag is a minor contributor (comparable to friction) to the dynamical balance of the ocean circulation over much of the globe, it is a significant player in the dynamics of extensive areas of the ocean (notably, the ACC and several regions of enhanced small-scale topographic variance in the equatorial and Southern Hemisphere oceans). There, the contribution of internal wave drag to the time-mean, full-depth balances of oceanic momentum, angular momentum, and vorticity is generally on the order of ten to a few tens of percent of (although less spatially

coherent than) the dominant source and sink terms in each dynamical budget, which are respectively associated with wind forcing and large-scale topographic form drag. To our knowledge, no direct measurements of internal wave momentum fluxes exist in these regions that may support or challenge the results presented here. Nonetheless, some indirect evidence of regionally enhanced internal lee wave activity is available, particularly in the ACC, that lends credence to our results. This evidence is found, for example, in the finestructure analyses of Naveira Garabato et al. (2004), Sloyan (2005) and Kunze et al. (2006), which suggest that elevated levels of internal wave energy and inferred turbulent dissipation are consistently present in wide sectors of the deep ACC overlying rough small-scale topography. Nikurashin and Ferrari (2010b) combine observations of the circulation and bathymetry in one of those sectors (Drake Passage) with wave radiation theory to show that the internal lee wave generation rate in the area is large enough to support the turbulent dissipation rates estimated by Naveira Garabato et al. (2004). A systematic intensification of internal wave energy and microstructure-derived turbulent dissipation within ACC jets is revealed by Waterman et al. (2013) in the ACC standing meander around the northern edge of the Kerguelen Plateau and by St. Laurent et al. (2012) in the ACC flow over the Phoenix Ridge in Drake Passage.

The significance of internal wave drag in the regions identified by our analysis echoes the findings of studies of the dynamical balance of the atmosphere. While form drag by large [horizontal scales in excess of  $O(100)$  km], essentially nonwave-radiating orographic obstacles has been argued to be the dominant sink of (angular) momentum in the time-varying atmospheric flow over a wide range of frequencies, internal wave drag (linked to orography with horizontal scales of 10–100 km) and friction have also been shown to make a substantial contribution, typically at the level of several tens of percent of the large-scale orographic form drag (see e.g., the reviews by Egger et al. 2007; Fritts and Alexander 2003, and references therein). It has been extensively shown that the inclusion (via parameterization) of internal wave drag in general circulation models of the atmosphere that do not resolve the wave-radiating scales leads to significant improvements in a range of important features of the atmospheric circulation, such as the structure of the winter jets, horizontal temperature gradients near the tropopause, and surface wind distributions (e.g., Alexander et al. 2010). If the atmospheric analogy holds in the regions highlighted here, we expect that the representation of internal wave drag in ocean general circulation models will lead to significant changes in the local deep ocean circulation, such as the

arrest of large-to-mesoscale geostrophic flows and the induction of ageostrophic secondary circulations as wave breaking deposits horizontal momentum away from the ocean floor. While the arrest of the ocean's geostrophic flow is made explicit in Figs. 4, 6, and 7, the ageostrophic effects of wave drag can be illustrated by considering the force balance of a deep ocean layer subject to wave drag,

$$f\hat{\mathbf{z}} \times \overline{\mathbf{u}}_a = -\rho_0^{-1} \frac{\partial \overline{\boldsymbol{\tau}}_{iw}}{\partial z}, \quad (12)$$

where  $\hat{\mathbf{z}}$  is the unit vector in the vertical direction and  $\overline{\mathbf{u}}_a$  is the time-mean horizontal ageostrophic velocity induced by the divergence of the vertical flux of horizontal momentum associated with internal lee waves. Substituting a value for  $|\overline{\boldsymbol{\tau}}_{iw}|$  characteristic of the ACC ( $\sim 0.05 \text{ N m}^{-2}$ ) and assuming a vertical scale  $O(1 \text{ km})$  (see e.g., Naveira Garabato et al. 2004), we obtain  $|\overline{\mathbf{u}}_a| \sim 0.5 \text{ mm s}^{-1}$ . Locally, this is comparable in magnitude to the zonally averaged ageostrophic velocities implicated in the meridional overturning circulation of the Southern Ocean ( $\sim 1 \text{ mm s}^{-1}$ , e.g., Hallberg and Gnanadesikan 2006), and thereby suggests that internal waves are likely to play a significant role in shaping the ageostrophic circulation in that and other regions where wave drag is of dynamical importance.

While the development of a parameterization is beyond the scope of this article, we propose that a reasonable strategy for such an effort is to represent (depth-integrated) internal wave drag by a quadratic law, as for frictional drag, but with a drag coefficient  $c_{iw}$  that is primarily dependent on topographic roughness, near-bottom flow speed and the Coriolis parameter,

$$|\boldsymbol{\tau}_{iw}| = \rho |\mathbf{u}|^2 c_{iw}, \quad (13)$$

where the possibly significant misalignment between the internal wave drag and the near-bottom velocity (Fig. 6) has been neglected. A detailed derivation of the dependence of  $c_{iw}$  on topographic and flow parameters is given in appendix B. This analysis yields that

$$c_{iw} \sim \tilde{h}_{rms}^2 G \frac{1}{2} \nu \pi^{-1/2} \frac{\Gamma\left(\nu - \frac{1}{2}\right)}{\Gamma(\nu + 1)} \frac{N}{f} \tilde{f}^{-2\nu+2} \mathbf{m} \cdot \hat{\mathbf{u}}, \quad (14)$$

where  $\tilde{h}_{rms} = h_{rms} \bar{k}$ ;  $\bar{k} = \sqrt{k_s k_n}$ ;  $G = |\boldsymbol{\tau}_{iw}| / |\boldsymbol{\tau}_{iw}|^{lim}$  [from Eq. (8)];  $\tilde{f} = |f|/|k|\mathbf{u}|$ ;  $\mathbf{m}$  is a vector function of  $\nu$ , topographic anisotropy, and flow orientation; and  $\hat{\mathbf{u}}$  is a unit vector in the direction of the flow. Expression (14) applies in the limit that  $\tilde{f} \gg 1$ , which is common in the mid- and high-latitude oceans. It reveals that, for the nonblocking condition  $G \sim 1$ —thought to hold widely in the ocean [section 2c(1)]— $c_{iw}$  is proportional to  $\tilde{h}_{rms}^2$  and

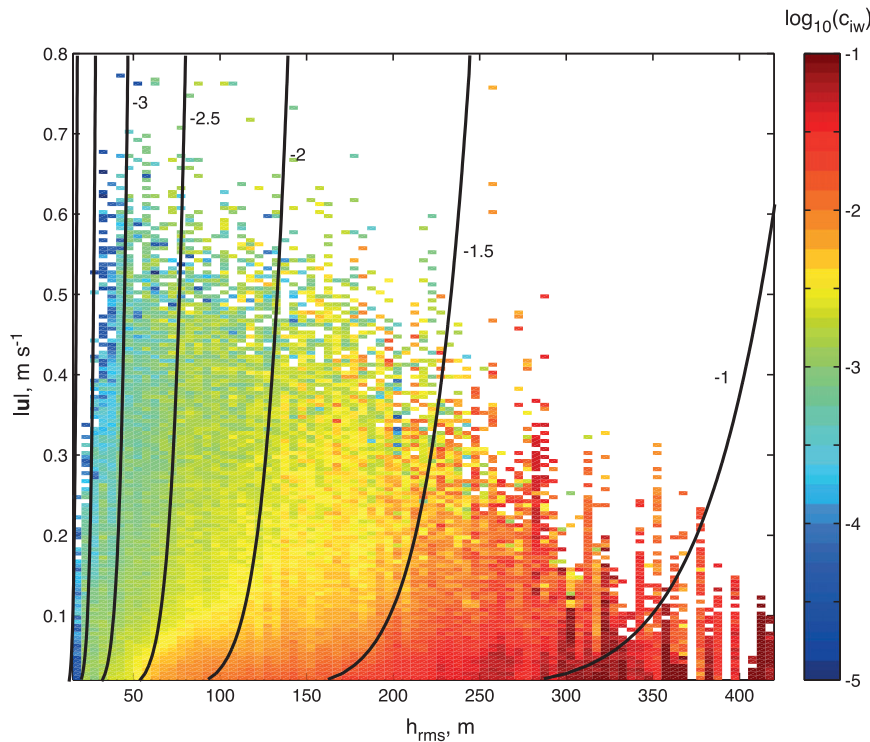


FIG. 9. Logarithm of the mean value of  $c_{iw}$  as a function of  $h_{rms}$  and the near-bottom speed for the calculations in this study (colors) and the scaling in (14) (contours). Characteristic values of  $G = 1$ ,  $\nu = 0.9$ ,  $N = 10^{-3} \text{ rad s}^{-1}$ ,  $f = 10^{-4} \text{ rad s}^{-1}$ ,  $k = 2 \times 10^{-4} \text{ rad m}^{-1}$ . A scaling factor of 2 (to account for  $\mathbf{m} \cdot \hat{\mathbf{u}}$ ) has been used in applying the scaling.

$|\mathbf{u}|^{-2(1-\nu)}$ , implying that  $|\boldsymbol{\tau}_{iw}|$  scales with  $h_{rms}^2$  and  $|\mathbf{u}|^{2\nu}$  (values of  $\nu$  range from 0.85 to 0.95 in the G2010 and GA2010 datasets). This scaling progressively fails as the flow becomes increasingly blocked by topography ( $G \ll 1$ ), in which case  $c_{iw}$  becomes independent of  $h_{rms}$ —or, as the flow speed increases such that  $\hat{f} \ll 1$ , the result is a far more pronounced decrease of  $c_{iw}$  with  $|\mathbf{u}|$  and an eventual decrease in  $|\boldsymbol{\tau}_{iw}|$ .

The extent to which the scaling (14) captures the dependence of the internal wave drag calculated in this study on topographic roughness and near-bottom flow speed is illustrated by Fig. 9, which shows the distribution of  $c_{iw}$  computed from (13) and binned as a function of  $h_{rms}$  and  $|\mathbf{u}|$  (in color) and the result of a simple application of the scaling in (14) using characteristic values of factors other than  $h_{rms}$  and  $|\mathbf{u}|$  (contours). It may be readily seen that the scaling captures the behavior of the numerical calculation of  $c_{iw}$  with reasonable accuracy over much of the  $h_{rms} - |\mathbf{u}|$  space. Note, for example, that at low  $|\mathbf{u}|$  the approximate quadratic dependence of  $c_{iw}$  on  $h_{rms}$  and the decelerated decrease of  $c_{iw}$  with increasing  $|\mathbf{u}|$  are both reflected in the scaling. The two limits outlined above in which the scaling performance deteriorates can also be gleaned from Fig. 9. Thus, the

dependence of  $c_{iw}$  on  $h_{rms}$  becomes less pronounced as blocking occurs more frequently, which tends to occur for combinations of relatively high  $h_{rms}$  (values of  $\sim 100$  m and greater) and  $|\mathbf{u}|$  (values in excess of  $\sim 0.2 \text{ m s}^{-1}$ ). Conversely, the dependence of  $c_{iw}$  on  $|\mathbf{u}|$  becomes more acute for high flow speeds (see, for example, the relatively rapid decrease of  $c_{iw}$  with  $|\mathbf{u}|$  for  $h_{rms} = 150$  m), as the limit  $\hat{f} \ll 1$  is approached.

*Acknowledgments.* ACNG acknowledges the support of a NERC Advanced Research Fellowship (NE/C517633/1) and a Philip Leverhulme Prize. We are grateful to Chris Hughes for providing us with the estimate of form drag by large-scale topography of Hughes and de Cuevas (2001), and to three anonymous reviewers for useful feedback on an earlier version of the manuscript.

## APPENDIX A

### Sensitivity of Internal Wave Drag Terms to the Calculation’s Input Parameter Choices

Our calculation of the contribution of internal wave drag to the depth-integrated (angular) momentum and

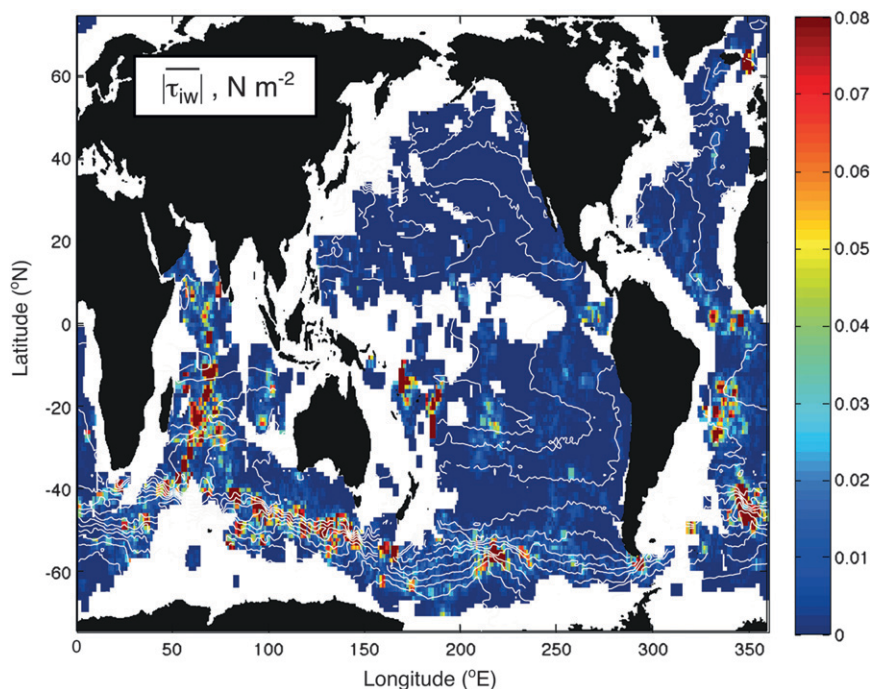


FIG. A1. Map of time-mean internal wave drag from a calculation using the GA2010 small-scale topographic dataset with other input parameters unchanged with respect to the default.

vorticity budgets is subject to several, somewhat subjective, parameter choices. In this appendix we assess the extent to which plausible variations of those parameters influence the calculation's results. We focus on quantifying the sensitivity of the climatological internal wave drag  $-\overline{\tau_{iw}}$  to such changes in input parameters, but examining the equivalent terms in the angular momentum and vorticity budgets leads to a very similar outcome. The choice of small-scale topographic dataset turns out to be the only one that affects the spatial distribution of  $\overline{\tau_{iw}}$  appreciably, whereas variations in other parameters are found to primarily impact the magnitude of  $\overline{\tau_{iw}}$  and not its spatial pattern. Consequently, we illustrate the calculation's sensitivity to the choice of small-scale topographic dataset with a map of  $-\overline{\tau_{iw}}$  estimated by replacing G2010 by GA2010 in the default calculation (i.e., the equivalent of Fig. 4a calculated from GA2010). Sensitivities to changes in other parameters are instead synthesized as the percentual change in  $|\overline{\tau_{iw}}|$  arising from changing one parameter at a time in the default calculation, averaged over the regions where internal wave drag is significant (defined as  $|\overline{\tau_{iw}}| > 0.01 \text{ N m}^{-2}$ ) in that default.

Figure A1 shows  $-\overline{\tau_{iw}}$  estimated from GA2010. When this figure is compared to Fig. 4a, it is readily apparent that both the magnitude and large-scale spatial distribution of the internal wave drag are rather insensitive to

the choice of small-scale topographic dataset. The magnitude of the internal wave drag is slightly larger on average (by  $\sim 10\%$ ) for GA2010 than in the default calculation, and the drag vector is generally directed in a similar direction (the rms difference in drag direction between the two estimates being  $19^\circ$  for regions where  $|\overline{\tau_{iw}}| > 0.01 \text{ N m}^{-2}$  in both calculations). The most significant difference between the two estimates is the absence of a clear enhancement of internal wave drag in the eastern equatorial Pacific in the calculation with the GA2010 dataset, which stems from the lack of resolution of the regional small-scale roughness in that dataset. Nonetheless, our general finding of internal wave drag representing a significant momentum sink (on the order of ten to a few tens of percent of the wind stress) in several regions or rough topography in the equatorial and Southern Hemisphere oceans stands.

The sensitivity of our estimate of internal wave drag to a range of other calculation input parameters [specifically, the use of near-bottom velocity data from different vertical levels and years of the DA simulation of HYCOM; the adoption of  $Fr_c^{-1} = 0.5$  in the correction for topographic blocking (8); and the neglect of that correction, such that  $\tau_{iw} = \tau_{iw}^{\text{in}}$ ] is also explored. The impact of such changes on the calculated drag is summarized in Table A1, which lists the percentual variation in  $|\overline{\tau_{iw}}|$  in each sensitivity experiment (changes in

TABLE A1. Experiments assessing the sensitivity of internal wave drag to a range of calculation input parameters, listing the percentage change in  $|\bar{\tau}_{iw}|$  arising from varying one parameter at a time in the default calculation, averaged over the regions where internal wave drag is significant (defined as  $|\bar{\tau}_{iw}| > 0.01 \text{ N m}^{-2}$  in the default). The sign of the percentage change indicates whether it is an increase or a decrease. ‘‘Level’’ refers to the HYCOM vertical level above the bathymetry from which the geostrophic flow field is extracted.

Level	Topography	Change in $ \bar{\tau}_{iw}(\%) $	Comments
2	G2010	n/a	Default
2	GA2010	+10	
1	G2010	−8	$\mathbf{u}$ in bottom boundary layer
3	G2010	+26	
2	G2010	−8	2004 flow field
2	G2010	−7	2005 flow field
2	G2010	+11	2007 flow field
2	G2010	+10	2008 flow field
2	G2010	−6	$\text{Fr}_c^{-1} = 0.5$
2	G2010	+11	$\tau_{iw} = \tau_{iw}^{\text{lin}}$

direction are minor or zero in all cases). All changes in the characteristic amplitude of internal wave drag are relatively modest, ranging between −8% and +26%,

with the larger figure associated with the use of velocity data from the third HYCOM level above the bathymetry. Thus, the overall inference from these sensitivity tests is that the results presented in this article are robust.

## APPENDIX B

### Dependence of Internal Wave Drag on Topographic Roughness, Flow Speed, and Coriolis Parameter

To gain insight into how a parameterization of internal wave drag may be developed in the future, we here show how the drag calculated from (6)–(10) varies with topographic roughness  $h_{\text{rms}}$ , near-bottom velocity, and the magnitude of the Coriolis parameter  $|f|$ . We commence by nondimensionalizing (6)–(10). First, wavenumber coordinates are rotated such that  $k \parallel \mathbf{u}$ , with  $U = |\mathbf{u}|$ . Then wavenumbers are scaled by the geometric mean of  $k_s$  and  $k_n$ :  $\tilde{k}, \tilde{l} = k/\bar{k}, l/\bar{k}$ , with  $\bar{k} = \sqrt{k_s k_n}$ ;  $|f|$ ,  $N$  and  $\sigma$  are scaled by  $\bar{k}U$ :  $\tilde{f}, \tilde{N}, \tilde{k} = |f|/(\bar{k}U), N/(\bar{k}U), \sigma/(\bar{k}U)$ ; and  $h_{\text{rms}}$  is scaled by  $(\bar{k}U)^{-1}$ , with  $\tilde{h}_{\text{rms}} = h_{\text{rms}}\bar{k}$ . This gives

$$-\tau_{iw}(x, y, t) = -\rho_0 U^2 \tilde{h}_{\text{rms}}^2 \frac{2G}{4\pi^2} \int_{\tilde{f}}^{\tilde{N}} \int_{-\infty}^{\infty} \frac{\tilde{\mathbf{k}}}{\sqrt{\tilde{k}^2 + \tilde{l}^2}} \tilde{P}(\tilde{k}, \tilde{l}) d\tilde{l} \sqrt{\tilde{N}^2 - \tilde{k}^2} \sqrt{\tilde{k}^2 - \tilde{f}^2} d\tilde{k}, \quad (\text{B1})$$

where the symmetry of the integrand over  $\tilde{k} \Leftrightarrow -\tilde{k}$  allows the replacement of the integral over the internal wave band  $\tilde{f} < |\tilde{k}| < \tilde{N}$  by twice the integral over  $\tilde{f} < \tilde{k} < \tilde{N}$ . Here  $G$  is the factor  $|\tau_{iw}|/|\tau_{iw}^{\text{lin}}|$  from (8), and the nondimensionalized topographic kernel is defined as

$$\begin{aligned} \tilde{P}(\tilde{k}, \tilde{l}) &= \bar{k}^4 \tilde{h}_{\text{rms}}^{-2} P(\tilde{k}, \tilde{l}) \\ &= 4\pi\nu \left\{ \tilde{\mathbf{k}}^2 \left[ \frac{k_n}{k_s} \cos^2(\theta - \theta_s) \right. \right. \\ &\quad \left. \left. + \frac{k_s}{k_n} \sin^2(\theta - \theta_s) \right] + 1 \right\}^{-(\nu+1)}, \quad (\text{B2a}) \end{aligned}$$

where  $\theta_s$  and  $\theta = \arctan(\tilde{k}/\tilde{l})$  are the azimuthal angles of the topographic strike and the wavenumber relative to the rotated coordinate frame in which  $\mathbf{u}$  is eastward. Expressed directly in terms of  $\tilde{k}$  and  $\tilde{l}$ ,

$$\tilde{P}(\tilde{k}, \tilde{l}) = 4\pi\nu \left[ \alpha \left( \tilde{l} + \frac{1}{2}\beta\alpha^{-1}\tilde{k} \right)^2 + \alpha^{-1}\tilde{k}^2 + 1 \right]^{-(\nu+1)}, \quad (\text{B2b})$$

where

$$\alpha = \varepsilon c^2 + \varepsilon^{-1} s^2; \quad \beta = 2sc(\varepsilon - \varepsilon^{-1}), \quad (\text{B2c})$$

and the topographic anisotropy

$$\varepsilon = k_n/k_s > 1 \quad \text{with} \quad (s, c) = (\sin\theta_s, \cos\theta_s). \quad (\text{B2d})$$

Figure B1 illustrates the distribution of  $\tilde{P}$  on the  $\tilde{k}, \tilde{l}$  plane, overlaid by the internal wave band  $\tilde{f} < \tilde{k} < \tilde{N}$ . It is worth emphasizing that the typically large oceanographic values of  $f/N \gtrsim 10$  imply that, unless  $\tilde{f}$  is small, there is little topographic kernel remaining over  $\tilde{k} > \tilde{N}$ .

#### a. Dependence on topographic roughness

The integrand in (B1) is independent of  $h_{\text{rms}}$ , so the roughness dependence of  $\tau_{iw}$  comes simply from the factor  $\tilde{h}_{\text{rms}}^2 G$ . So,  $\tau_{iw} \propto h_{\text{rms}}^2$  until the Froude number cutoff factor  $G$  (8) starts to operate, when  $\text{Fr}^{-1} = NHU^{-1} > \text{Fr}_c^{-1} = 0.7$ , where  $H$  is the ‘‘effective’’ height given by (9). Writing

$$H = \eta h_{\text{rms}}, \quad (\text{B3})$$

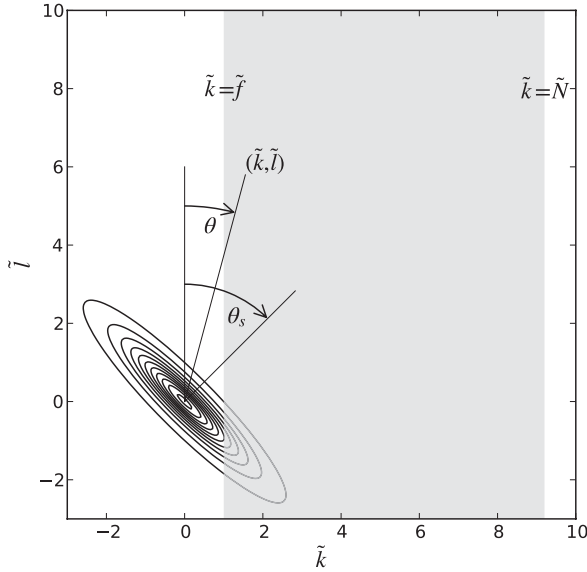


FIG. B1. Scaled topography  $\tilde{P}$  (contours, CI = 1) and internal wave zone  $\tilde{f} < \tilde{k} < \tilde{N}$  (shaded) in a reference frame in which the scaled wavenumbers  $(\tilde{k}, \tilde{l})$  have been rotated so that  $\tilde{k}$  is aligned with the near-bottom velocity. Azimuths  $\theta_s$  of the strike and  $\theta$  of the wavenumber are relative to the rotated  $\tilde{l}$  axis.

the ratio  $\eta$  is found by nondimensionalizing (9), again using the symmetry of the integrand over  $\tilde{k} \leftrightarrow -\tilde{k}$ :

$$\eta^2 = \frac{2}{4\pi^2} \int_{\tilde{f}}^{\tilde{N}} \int_{-\infty}^{\infty} \tilde{P}(\tilde{k}, \tilde{l}) d\tilde{l} d\tilde{k}. \quad (\text{B4})$$

Note that the effective height  $H$  is always less than the rms height  $h_{\text{rms}}$  ( $0 < \eta < 1$ ) and that  $\eta$  is independent of  $h_{\text{rms}}$ . Hence the cutoff operates for

$$Nh_{\text{rms}}U^{-1} > \text{Fr}_c^{-1}\eta^{-1} > \text{Fr}_c^{-1}. \quad (\text{B5})$$

For larger  $h_{\text{rms}}$  giving  $\text{Fr}^{-1} \gg \text{Fr}_c^{-1}$ , equivalent to  $L \equiv \text{FrFr}_c^{-1} \ll 1$  in (8),  $G \sim L^2$ , so

$$\tilde{h}_{\text{rms}}^2 G \sim h_{\text{rms}}^2 \tilde{k}^2 U^2 N^{-2} H^{-2} \text{Fr}_c^{-2} \sim \tilde{N}^{-2} \eta^{-2} \text{Fr}_c^{-2} \quad (\text{B6})$$

and  $\tau_{\text{iw}}$  no longer depends on  $h_{\text{rms}}$ .

If it were the case that  $H \approx h_{\text{rms}}$ ,  $\eta \approx 1$ , then for, for example, bottom buoyancy frequency  $N = 10^{-3} \text{ rad s}^{-1}$ ,  $U = 0.1 \text{ m s}^{-1}$ , the cutoff would start to operate when  $h_{\text{rms}} = 70 \text{ m}$  (top left edge of gray band in Fig. B2), and reduce  $|\tau_{\text{iw}}|$  by a factor of 2 [where  $L \equiv \text{FrFr}_c^{-1} \approx 1.4$  in Eq. (8) for  $G$ ] when  $h_{\text{rms}} \approx 100 \text{ m}$  (bottom right edge of gray band). However, generally away from the equator (see below)  $\eta \ll 1$ , so the Froude number cutoff is only attained for much larger  $h_{\text{rms}}$ : for example, with the preceding values of  $N$  and  $U$ , for  $f = 5 \times 10^{-5} \text{ s}^{-1}$ ,  $h_{\text{rms}}$

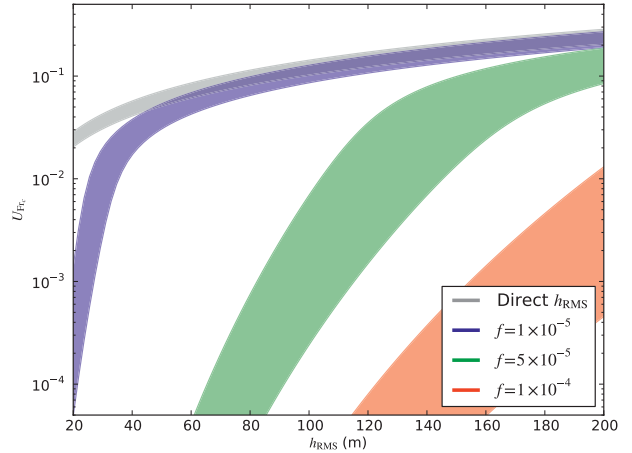


FIG. B2. Values of  $U$  and  $h_{\text{rms}}$  that give  $\text{Fr}^{-1} = \text{Fr}_c^{-1} = 0.7$  (the upper edge of the colored regions) and  $\text{Fr}^{-1} = 1.4\text{Fr}_c^{-1} = 0.98$  (the lower edge of the colored regions, for which the topographic blocking factor used in (8) reduces the internal wave drag from its linear value  $\tau_{\text{iw}}^{\text{lin}}$  by a factor of 2).

must reach 140 m (left/top edge of green band in Fig. B2). For typical Southern Ocean values of  $f \sim 10^{-4} \text{ s}^{-1}$ , attaining the cutoff may require extremely large  $h_{\text{rms}} \sim 300 \text{ m}$  (red band in Fig. B2). As the equator is approached (e.g.,  $f = 10^{-5} \text{ s}^{-1}$ ), though,  $\eta \sim 1$  and the Froude number cutoff occurs much earlier (blue band in Fig. B2).

By expressing  $\tilde{P}$  explicitly in terms of  $\tilde{k}$  and  $\tilde{l}$  (B2b), integrating over  $\tilde{l}$  using the integral representation of the beta function [e.g., Abramowitz and Stegun (1972), p. 258, Eqs. (6.2.1) and (2)], and then integrating over  $\tilde{k}$  by considering the integral representation of the Gauss hypergeometric function  ${}_2F_1(a, b; c; z)$  [e.g., Abramowitz and Stegun (1972); p. 558, Eq. (15.3.6)], the integral (B4) may be expressed in closed form:

$$\eta^2 = J(\tilde{N}a^{-1}) - J(\tilde{f}a^{-1}), \quad (\text{B7a})$$

where the orientation of the strike relative to the velocity and the topographic anisotropy  $\varepsilon = k_n/k_s$  (B2d) control the parameter

$$a^2 = \alpha = \varepsilon \cos^2 \theta_s + \varepsilon^{-1} \sin^2 \theta_s, \quad (\text{B7b})$$

and the function  $J$  is defined in terms of the Hurst number  $\nu$  and the gamma function by

$$J(x) = \frac{2\Gamma(\nu + 1/2)}{\pi^{1/2}\Gamma(\nu)} {}_2F_1(1/2, \nu + 1/2; 3/2; -x^2). \quad (\text{B7c})$$

This  $J(x)$  is monotonically increasing with

$$J(x) \sim \begin{cases} x & \text{for small } x, \\ 1 - \pi^{-1/2} \Gamma(\nu + 1/2) \Gamma(\nu)^{-1} \nu^{-1} x^{-2\nu} & \text{as } x \rightarrow \infty. \end{cases} \quad (\text{B7d})$$

Typically the topographic parameter  $a$  defined in (B7b) is  $O(1)$ ; for example, for  $\varepsilon = k_n/k_s = 5$ ,  $a$  decreases from  $\sim 2.24$  (flow across topography,  $\perp$  strike) to  $0.45$  (flow along topography,  $\parallel$  strike). However,  $\tilde{N}$  is large ( $\sim 45$  for  $N = 10^{-3} \text{ s}^{-1}$ ,  $\tilde{k} = 2.2 \times 10^{-4} \text{ m}^{-1}$ ,  $U = 0.1 \text{ m s}^{-1}$ ), so  $J(\tilde{N}a^{-1}) \sim 1$ . At the equator  $f = 0$ , so  $\eta \sim 1$ : physically, the shaded internal wave band  $\tilde{f} < \tilde{k} < \tilde{N}$  in Fig. B1 covers everywhere where the topographic kernel  $P(\tilde{k}, \tilde{l})$  is significant. Yet, in the subtropics and midlatitudes ( $f = 5 \times 10^{-5} \text{ s}^{-1}$ ,  $f = 10^{-4} \text{ s}^{-1}$ ),  $\tilde{f} \sim 2.5$  and  $\sim 5$  is large enough that much of the strongest topographic kernel lies outside the internal wave band. For flow directed at  $45^\circ$  to the strike, as described in Fig. B2, the above  $k_n/k_s = 5$  gives  $a \approx 1.61$ , thus with the preceding parameters,  $\eta \sim 0.47$  and  $\sim 0.27$ , respectively, implying Froude cutoffs starting at  $\sim 149 \text{ m}$  and  $\sim 260 \text{ m}$ . Even for flow “across” the topography,  $\tilde{f}a^{-1} \sim 1$  and  $\sim 2$ , giving  $\eta \sim 0.57$  and  $\sim 0.36$ . Of course, for weaker  $U$ , where the Froude number cutoff might be expected to be more significant,  $\tilde{f}$  becomes even larger and  $\eta$  even smaller. The consequence is that the Froude number cutoff is mostly not attained, so for fixed  $U$ ,  $f$ , and  $N$   $\tau_{\text{iw}} \propto h_{\text{rms}}^2$  is a good assumption.

*b. Dependence on flow velocity and Coriolis parameter*

The dependence of  $-\tau_{\text{iw}}$  in (B1) on  $\mathbf{u}$  is both explicit, from the  $U^2$  factor, and implicit from the dependence of the integral in (B1) on  $\mathbf{u}$  through  $\tilde{N}$ ,  $\tilde{f}$  and  $\theta_s$ . We write

$$-\tau_{\text{iw}} = -\rho U^2 c_{\text{iw}} \mathbf{R} \hat{\mathbf{u}}, \quad (\text{B8})$$

where  $c_{\text{iw}}$  is the IW drag coefficient,  $\mathbf{R}$  is a rotation tensor, and  $\hat{\mathbf{u}}$  is the unit vector,  $\mathbf{u} = U \hat{\mathbf{u}}$ . We then focus on the velocity dependence of this “vector drag coefficient”

$$c_{\text{iw}} \sim 2 \tilde{h}_{\text{rms}}^2 G \nu \pi^{-1} \int_{\tilde{f}}^{\tilde{N}} \int_{-\infty}^{\infty} \frac{(1, l')}{\sqrt{1 + l'^2}} \left[ \alpha \left( \tilde{l}' + \frac{1}{2} \beta \alpha^{-1} \tilde{k} \right)^2 + \alpha^{-1} \tilde{k}^2 \right]^{-(\nu+1)} dl' \times \tilde{k}^{-2\nu-1} \sqrt{\tilde{N}^2 - \tilde{k}^2} \sqrt{\tilde{k}^2 - \tilde{f}_0^2} d\tilde{k}.$$

Now the integral over  $l'$  is a (vector) function solely of the topographic anisotropy  $\varepsilon$ , the azimuth of the strike relative to the flow  $\theta_s$ , and the Hurst parameter  $\nu$ . We write this as  $\mathbf{m}(\theta_s, \varepsilon, \nu)$ —it is independent of both  $\tilde{k}$  and the flow speed  $U$ . Additionally, we assume that  $\tilde{N}$  is

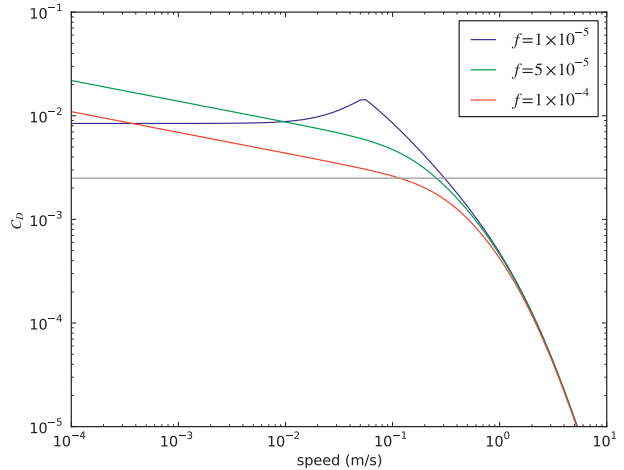


FIG. B3. Dependence of the internal wave drag coefficient  $c_{\text{iw}}$  on near-bottom speed (for a velocity at  $45^\circ$  to the strike direction) for three values of  $f$  and for near-bottom buoyancy frequency  $N = 10^{-3} \text{ rad s}^{-1}$ , strike wavenumber  $k_s = 10^{-4} \text{ rad m}^{-1}$ , normal wavenumber  $k_n = 5 \times 10^{-4} \text{ rad m}^{-1}$ , and Hurst parameter  $\nu = 0.9$ .

$\mathbf{c}_{\text{iw}} = c_{\text{iw}} \mathbf{R} \hat{\mathbf{u}}$ . This dependence is, in general, complex and can only be determined by numerical integration of (B1). However, for the relatively large  $\tilde{f}$  typical of midlatitudes and characteristic bottom velocities, the only part of the topographic kernel within the internal wave band has  $\tilde{k} \gg 1$ , and we can approximate the kernel (B2b) by

$$\tilde{P}(\tilde{k}, \tilde{l}) \sim 4\pi\nu \left[ \alpha \left( \tilde{l} + \frac{1}{2} \beta \alpha^{-1} \tilde{k} \right)^2 + \alpha^{-1} \tilde{k}^2 \right]^{-(\nu+1)}$$

so that, writing  $l' = \tilde{l}/\tilde{k}$ ,

$$\sim 4\pi\nu \tilde{k}^{-2(\nu+1)} \left[ \alpha \left( \tilde{l}' + \frac{1}{2} \beta \alpha^{-1} \right)^2 + \alpha^{-1} \right]^{-(\nu+1)}.$$

Also, eliminating  $\tilde{l}$  in  $\tilde{k}/\sqrt{(\tilde{k}^2 + \tilde{l}^2)}$  in favor of  $l'$ , it follows that

large enough that the topographic kernel is insignificant for  $\tilde{k} \sim \tilde{N}$ , so (i) we can replace  $\tilde{N}$  by  $\infty$  as the upper bound of the  $\tilde{k}$  integral and (ii) replace  $\sqrt{\tilde{N}^2 - \tilde{k}^2}$  by  $\tilde{N}$  in the integrand. Rewriting  $\tilde{k} = \tilde{f} k'$  in the  $\tilde{k}$  integral:

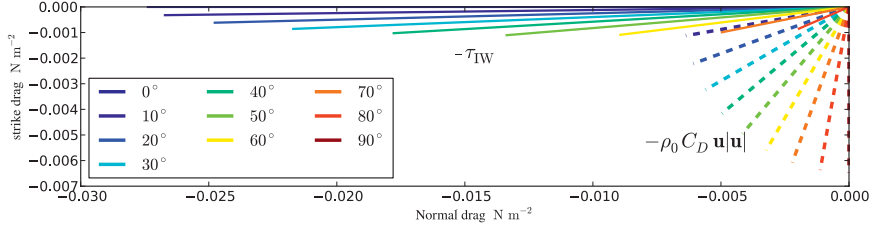


FIG. B4. Comparison of internal wave drag  $-\tau_{iw}$  with quadratic bottom drag (with  $c_d = 2.5 \times 10^{-3}$ ) for a near-bottom speed  $5 \text{ cm s}^{-1}$  and strike orientations ranging from  $0^\circ$  ( $\perp$  to flow) to  $90^\circ$  ( $\parallel$  to the flow). Values of other parameters are  $f = 10^{-5} \text{ s}^{-1}$ ,  $h_{\text{rms}} = 50 \text{ m}$ , and  $\nu = 0.9$ .

$$\begin{aligned} \mathbf{c}_{iw} &\sim 2\tilde{h}_{\text{rms}}^2 G \nu \pi^{-1} \mathbf{m}(\theta_s, \varepsilon, \nu) \tilde{N} \tilde{f}^{-2\nu+1} \\ &\quad \times \int_1^i k'^{-2(\nu+1)} \sqrt{k'^2 - 1} dk' \\ &\sim \tilde{h}_{\text{rms}}^2 \times G \frac{1}{2} \nu \pi^{-1/2} \frac{\Gamma(\nu - 1/2)}{\Gamma(\nu + 1)} \mathbf{m}(\theta_s, \varepsilon, \nu) \frac{N}{\tilde{f}} \tilde{f}^{-2\nu+2}, \end{aligned} \quad (\text{B9})$$

again using the integral representation of the beta function to evaluate the  $k'$  integral. Since  $\tilde{f} = f/(U\bar{k})$ , (B9) predicts a  $U^{-2(1-\nu)}$  dependency of  $\mathbf{c}_{iw}$  over parameter space where  $\tilde{f} \gg 1$ .

Figure B3 displays the component of the “vector” internal wave drag coefficient in the flow direction,  $\mathbf{c}_{iw} \cdot \hat{\mathbf{u}}$  against near-bottom speed (for a velocity at  $45^\circ$  to the strike direction) for various values of  $f$  and for typical near-bottom buoyancy frequency  $N = 10^{-3} \text{ rad s}^{-1}$ , strike wavenumber  $k_s = 10^{-4} \text{ m}^{-1}$ , normal wavenumber  $k_n = 5 \times 10^{-4} \text{ m}^{-1}$ , and Hurst parameter  $\nu = 0.9$ . Note the general decrease of  $c_{iw}$  with increasing speed, also evident in Fig. 9. However, the striking feature is that for weak velocities and mid-latitude values of  $f$  ( $5 \times 10^{-5} \text{ s}^{-1}$  and  $10^{-4} \text{ s}^{-1}$ ),  $c_{iw}$  varies like  $U^{-0.2}$ , in agreement with (B9), given the value of  $\nu$ .

The flat  $c_{iw}$  evident for small  $U$  and equatorial value of  $f = 10^{-5} \text{ s}^{-1}$  is the Froude cutoff regime. For  $\tilde{N} \gg 1$ , and “large”  $\tilde{f}$ , we have from (B7d) that

$$\eta^2 \sim 1 - J(\tilde{f}a^{-1}) \sim \pi^{-1/2} \Gamma(\nu + 1/2) \Gamma(\nu)^{-1} \nu^{-1} (\tilde{f}a^{-1})^{-2\nu}.$$

Using the Eq. (B6) for  $\tilde{h}_{\text{rms}}^2 G$ , when  $\text{Fr}^{-1} \gg \text{Fr}_c^{-1}$ , and substituting into (B9) gives the  $U$ -independent value

$$\mathbf{c}_{iw} \sim \text{Fr}_c^{-2} \frac{\nu}{2\nu - 1} a^{-2\nu} \mathbf{m}(\theta_s, \varepsilon, \nu) \frac{f}{N}. \quad (\text{B10})$$

Although the linear drag decreases  $\sim f^{-2\nu+1}$  with increasing  $f$  (B9), paradoxically, because the cutoff is

attained at lower speeds for larger Coriolis parameter, the value of the cutoff drag (B10) increases with  $f$ .

Asymptotic limits for  $c_{iw}$  when  $U$  is large are difficult to obtain. We content ourselves here with mentioning that, as  $U$  increases,  $\tilde{f}$  and even  $\tilde{N}$  both decline, so the area in  $\tilde{k} - \tilde{l}$  space of the internal wave band reduces  $\propto U^{-1}$ . Additionally, the maximum of the product of the square roots  $\sqrt{\tilde{N}^2 - \tilde{k}^2} \sqrt{\tilde{k}^2 - \tilde{f}^2} \sim \tilde{N}^2 - (1/2)(\tilde{N} + \tilde{f})^2$  reduces  $\propto U^{-2}$ . The resulting  $\propto U^{-3}$  behavior is counterbalanced somewhat by the larger values of the topographic kernel as the internal wave band approaches the origin, but close to the origin (very large  $U$ ) these stop increasing and the steep decline of  $c_{iw}$  implies even that the internal wave drag itself declines as  $U$  increases. This accelerating decrease in  $c_{iw}$  with large  $U$  is evident in Fig. B3.

### c. Variation of internal wave drag with strike angle

The anisotropy of the topography causes the internal wave drag to tend to be aligned along the normal direction of the topography, the direction along which the topography varies most strongly, rather than directly opposing the flow. This anisotropy is typically significant, and the value  $\varepsilon = k_n/k_s = 5$  chosen in the earlier examples in this appendix is not atypical (Scott et al. 2011). Unfortunately, the part of the integral that relates to the flow/topography orientation is not analytically tractable. In Fig. B4 we simply show how the numerically evaluated  $-\tau_{iw}$  varies for different orientations of a bottom speed of  $0.05 \text{ m s}^{-1}$ , with the standard parameters used here:  $f = 10^{-4} \text{ s}^{-1}$ ,  $h_{\text{rms}} = 50 \text{ m}$ ,  $\nu = 0.9$ , and  $\varepsilon = 5$ . The different colored lines show the (vector) internal wave drag for different angles of the flow relative to the normal direction of the topography, and the corresponding dashed lines the quadratic bottom drag, with opposite sense to the bottom flow, for a typical  $c_d = 2.5 \times 10^{-3}$ . It is striking how strongly aligned the  $\tau_{iw}$  is along the normal direction of the topography.

## REFERENCES

- Abramowitz, M., and I. Stegun, Eds., 1972: *Handbook of Mathematical Functions with Formulas, Graphs, and Mathematical Tables*. Applied Mathematics Series, Vol. 55, National Bureau of Standards, 1046 pp.
- Alexander, M. J., and Coauthors, 2010: Recent developments in gravity-wave effects in climate models and the global distribution of gravity-wave momentum flux from observations and models. *Quart. J. Roy. Meteor. Soc.*, **136**, 1103–1124.
- Antonov, J. I., R. A. Locarnini, T. P. Boyer, A. V. Mishonov, and H. E. Garcia, 2006: *Salinity*. Vol. 2, *World Ocean Atlas 2005*, S. Levitus, Ed., NOAA Atlas NESDIS 62, 182 pp.
- Bacmeister, J. T., and R. T. Pierrehumbert, 1988: On the high-drag states of nonlinear stratified flow over an obstacle. *J. Atmos. Sci.*, **45**, 63–80.
- Bell, T. H., 1975: Topographically generated internal waves in the open ocean. *J. Geophys. Res.*, **80**, 320–327.
- Eckermann, S. D., J. Lindeman, D. Broutman, J. Ma, and Z. Boybeyi, 2010: Momentum fluxes of gravity waves generated by variable Froude number flow over three-dimensional obstacles. *J. Atmos. Sci.*, **67**, 2260–2278.
- Eden, C., and D. Olbers, 2009: Why western boundary currents are diffusive: A link between bottom pressure torque and bolus velocity. *Ocean Modell.*, **32**, 14–24.
- Egger, J., K. Weickmann, and K.-P. Hoinka, 2007: Angular momentum in the global atmospheric circulation. *Rev. Geophys.*, **45**, RG4007, doi:10.1029/2006RG000213.
- Ferrari, R., and C. Wunsch, 2009: Ocean circulation kinetic energy: Reservoirs, sources and sinks. *Annu. Rev. Fluid Mech.*, **41**, 253–282.
- Fritts, D. C., and M. J. Alexander, 2003: Gravity wave dynamics and effects in the middle atmosphere. *Rev. Geophys.*, **41**, 1003, doi:10.1029/2001RG000106.
- Gill, A. E., 1982: *Atmosphere–Ocean Dynamics*. Academic Press, 662 pp.
- Goff, J. A., 2010: Global prediction of abyssal hill root-mean-square heights from small-scale altimetric gravity variability. *J. Geophys. Res.*, **115**, B12104, doi:10.1029/2010JB007867.
- , and T. H. Jordan, 1988: Stochastic modeling of seafloor morphology: Inversions of sea beam data for second-order statistics. *J. Geophys. Res.*, **93** (B11), 13 589–13 608.
- , and T. Jordan, 1989: Stochastic modeling of seafloor morphology: A parameterized gaussian model. *Geophys. Res. Lett.*, **16**, 45–48.
- , and B. K. Arbic, 2010: Global prediction of abyssal hill roughness statistics for use in ocean models from digital maps of paleo-spreading rate, paleo-ridge orientation, and sediment thickness. *Ocean Modell.*, **32**, 36–43.
- , B. E. Tucholke, J. Lin, G. E. Jaroslow, and M. C. Kleinrock, 1995: Quantitative analysis of abyssal hills in the Atlantic Ocean: A correlation between inferred crustal thickness and extensional faulting. *J. Geophys. Res.*, **100**, 22 509–22 522.
- , Y. Ma, A. Shah, J. R. Cochran, and J. C. Sempere, 1997: Stochastic analysis of seafloor morphology on the flank of the Southeast Indian Ridge: The influence of ridge morphology on the formation of abyssal hills. *J. Geophys. Res.*, **102** (B7), 15 521–15 534.
- Hallberg, R. W., and A. Gnanadesikan, 2006: The role of eddies in determining the structure and response of the wind-driven Southern Hemisphere overturning: Results from the modeling eddies in the Southern Ocean (MESO) project. *J. Phys. Oceanogr.*, **36**, 2232–2252.
- Hughes, C. W., and B. A. de Cuevas, 2001: Why western boundary currents in realistic oceans are inviscid: A link between form stress and bottom pressure torques. *J. Phys. Oceanogr.*, **31**, 2871–2885.
- Kasahara, A., 2010: A mechanism of deep-ocean mixing due to near-inertial waves generated by flow over bottom topography. *Dyn. Atmos. Oceans*, **49**, 124–140.
- Kunze, E., E. Firing, J. M. Hummon, T. K. Chereskin, and A. M. Thurnherr, 2006: Global abyssal mixing inferred from lowered ADCP shear and CTD strain profiles. *J. Phys. Oceanogr.*, **36**, 1553–1576.
- Locarnini, R. A., A. V. Mishonov, J. I. Antonov, T. P. Boyer, and H. E. Garcia, 2006: *Temperature*. Vol. 1, *World Ocean Atlas 2005*, S. Levitus, Ed., NOAA Atlas NESDIS 61, 182 pp.
- Lu, Y. Y., and D. Stammer, 2004: Vorticity balance in coarse-resolution global ocean simulations. *J. Phys. Oceanogr.*, **34**, 605–622.
- McCartney, M. S., 1975: Inertial Taylor columns on a beta plane. *J. Fluid Mech.*, **68**, 71–95.
- Munk, W. H., 1950: On the wind-driven ocean circulation. *J. Meteor.*, **7**, 79–93.
- Naveira Garabato, A. C., K. L. Polzin, B. A. King, K. J. Heywood, and M. Visbeck, 2004: Widespread intense turbulent mixing in the Southern Ocean. *Science*, **303**, 210–213.
- Nikurashin, M., and R. Ferrari, 2010a: Radiation and dissipation of internal waves generated by geostrophic motions impinging on small-scale topography: Theory. *J. Phys. Oceanogr.*, **40**, 1055–1074.
- , and —, 2010b: Radiation and dissipation of internal waves generated by geostrophic motions impinging on small-scale topography: Application to the Southern Ocean. *J. Phys. Oceanogr.*, **40**, 2025–2042.
- , and —, 2011: Global energy conversion rate from geostrophic flows into internal lee waves in the deep ocean. *Geophys. Res. Lett.*, **38**, L08610, doi:10.1029/2011GL046576.
- Peltier, W. R., and T. L. Clark, 1979: The evolution and stability of finite amplitude mountain waves. Part II: Surface wave drag and severe downslope windstorms. *J. Atmos. Sci.*, **36**, 1498–1529.
- Rosmond, T. E., J. Teixeira, M. Peng, T. F. Hogan, and R. Pauley, 2002: Navy Operational Global Atmospheric Prediction System (NOGAPS): Forcing for ocean models. *Oceanography (Wash. D.C.)*, **15**, 99–108.
- Scott, R. B., B. K. Arbic, E. P. Chassignet, A. C. Coward, M. Maltrud, W. J. Merryfield, A. Srinivasan, and A. Varghese, 2010: Total kinetic energy in four global eddying ocean circulation models and over 5000 current meter records. *Ocean Modell.*, **32**, 157–169.
- , J. A. Goff, A. C. Naveira Garabato, and A. G. J. Nurser, 2011: Global rate and spectral characteristics of internal gravity wave generation by geostrophic flow over topography. *J. Geophys. Res.*, **116** (C9), doi:10.1029/2011JC007005.
- Siefridt, L., and B. Barnier, 1993: Banque de Données AVISO Vent/flux: Climatologie des analyses de surface du CEP-MMT. IFREMER Tech. Rep. 91, 43 pp.
- Sloyan, B. M., 2005: Spatial variability of mixing in the Southern Ocean. *Geophys. Res. Lett.*, **32**, L18603, doi:10.1029/2005GL023568.
- Smith, K. S., 2007: The geography of linear baroclinic instability in Earth's oceans. *J. Mar. Res.*, **65**, 655–683.

- Smith, W. H. F., and D. T. Sandwell, 2004: Conventional bathymetry, bathymetry from space, and geodetic altimetry. *Oceanography*, **17**, 8–23.
- St. Laurent, L., A. C. Naveira Garabato, J. R. Ledwell, A. M. Thurnherr, J. M. Toole, and A. J. Watson, 2012: Turbulence and diapycnal mixing in Drake Passage. *J. Phys. Oceanogr.*, **42**, 2143–2152.
- Stommel, H., 1948: The westward intensification of wind-driven ocean currents. *Trans. Amer. Geophys. Union*, **29**, 202–206.
- Vallis, G. K., 2006: *Atmospheric and Oceanic Fluid Dynamics*. Cambridge University Press, 745 pp.
- Waterman, S. N., A. C. Naveira Garabato, and K. L. Polzin, 2013: Internal waves and turbulence in the Antarctic Circumpolar Current. *J. Phys. Oceanogr.*, **43**, 259–282.
- Webb, D. J., B. A. de Cuevas, and A. C. Coward, 1998: The first main run of the OCCAM global ocean model. Southampton Oceanography Centre Internal Doc. 34, 43 pp.
- Welch, W. T., P. K. Smolarkiewicz, R. Rotunno, and B. Boville, 2001: The large-scale effects of flow over periodic mesoscale topography. *J. Atmos. Sci.*, **58**, 1477–1492.
- Wells, H., S. B. Vosper, A. N. Ross, A. R. Brown, and S. Webster, 2008: Wind direction effects on orographic drag. *Quat. J. Roy. Meteor. Soc.*, **134**, 689–701.